A spatial light modulator for ion trapping experiments

Ein räumlicher Lichtmodulator für Experimente in Ionenfallen

Sebastian Schunke
Ludwig-Maximilians Universität München
May 26, 2015

Supervisors

Prof. Dr. Rainer Blatt

Prof. Dr. Harald Weinfurter

Leopold-Franzens Universität
Innsbruck

Ludwig-Maximilians-Universität
München

Contents

Chapter 1

Introduction

Computers have come a long way since the first machines like Zuse's Z4 and the ENIAC. Today's microprocessor computers can calculate millions of digits of π, forecast the weather or render three dimensional environments for video games. Even modern cell phones are more powerful than the computer that brought Apollo 11 to the moon and back. Yet there are problems which are hard to solve, even for the best computers and sometimes we even rely on this fact. The high difference in difficulty between the multiplication of numbers and its reverse, the finding of a number's prime factors is the basis of modern encryption technology.

While this seems like a topic that only spies would be interested in, other problems are of more general interest. Calculating properties of solids, such as magnetism and superconductivity is of great interest for material sciences, however today systems of no more than a few dozen atoms or electrons can be simulated. While this allows some insight into the properties of many body systems it is of course far from predicting bulk properties. Problems like these are the target of *quantum information* research. With ever increasing control over isolated quantum systems scientists are trying to build machines, that allow the simulation of complex systems, which go beyond the capabilities of modern supercomputers. It may yet take some time for quantum computers to factorize numbers, which are relevant for encryption purposes, in the regime of simulations however, experiments are slowly leaving the realm of proof of principle and are approaching the problems which are still unsolved.

To achieve these incredible feats precise control over experimental parameters is necessary. Ultra stable lasers, with linewidths of less than 1Hz have become so common that implementing them is now the topic of master's theses. But not only spectral properties of light are important for experimental control. Single particle addressing through high-NA optics is just as elementary as uniform illumination of many particles at the same time.

This thesis introduces and characterizes an optoelectronic device, which can further raise the level of experimental control, by correcting optical aberrations, as well as being able to create almost arbitrary patterns of light.

In the following chapters the theoretical background for the operation of this device is introduced. The theory of diffraction and Fourier optics is presented in chapter 3 and the device itself and its principle of operation are introduced in chapter 4. Chapter 5 presents several experimental results, such as the calibration of the device and characterization of its capabilities in terms of beam-shaping and aberration correction. The thesis concludes with a summary of the results and a suggested setup to integrate the device with the current ion trap setup of our group.

Chapter 2

Quantum Information with trapped ions

This chapter briefly introduces the foundations of quantum information technology and the approach through trapped atomic ions. It shall serve as a motivation for the following work.

2.1 Quantum Simulation

The theory of quantum mechanics has revolutionized our understanding of the world. But not only the scientific world has profited from the development of this strange theory [12] [17]. However, only in the beginning of the 1980s scientists started to seriously think about manipulating individual quantum systems in order to process information or gain information about *another* system [5] [2]. The notion of universal processing of information information, where one device can perform any task, is known as quantum computation, while the idea of gaining information about quantum systems, which are hard to calculate, by emulating them with well controlled systems is called quantum simulation. By inspecting differences between classical computers and their quantum counterparts the power of quantum information becomes more visible.

2.1.1 The Qubit

In classical information processing the basic building block of information is the *bit*. It can take either of two states, usually denoted as 0 and 1. The actual implementation of a bit is not attached to a single physical quantity and can be achieved in many ways, but it is very often connected to electronic quantities such as current and voltage, e.g a current flowing through a transistor signifying "1" and no current flowing signifying "0". A classical bit can only occupy one of its possible states at the same time, even if the quantity used to implement the bit is continuous, like a voltage. In the quantum world the

situation is profoundly changed. If one considers a quantum mechanical system of two states (a two-level system), one must consider the unique properties of quantum mechanics. Let the two states be denoted in the bra-ket formalism of Paul Dirac as $|0\rangle$ and $|1\rangle$. Now, in contrast to the classical bit, the state of the two-level system can be in arbitrary superpositions of its basis states:

$$|\Psi\rangle = c_0 |0\rangle + c_1 |1\rangle \tag{2.1}$$

where c_0 and c_1 are complex coefficients, bound by the condition $|c_0|^2 + |c_1|^2 = 1$. These coefficients can, be explicitly written as

$$|\Psi\rangle = e^{i\gamma} \left(\cos\frac{\theta}{2} |0\rangle + e^{i\phi} \sin\frac{\theta}{2} |1\rangle \right) \tag{2.2}$$

with γ, θ and ϕ now real numbers.

While different representations are perfectly possible, this one gives rise to a special visualization of a qubit's state. Since the global phase γ does not influence any measurement outcomes it can be neglected by setting it equal to zero. The parameters θ and ϕ can now be interpreted as spherical coordinates and give rise to the picture of the Bloch sphere. (Fig. 2.1) In this representation two states whose vectors point to opposite sides of the sphere are orthonormal. That is to say, that against the usual intuition points on opposing sides have a zero scalar product, while points with relative angle equal to $\pi/2$ do not.
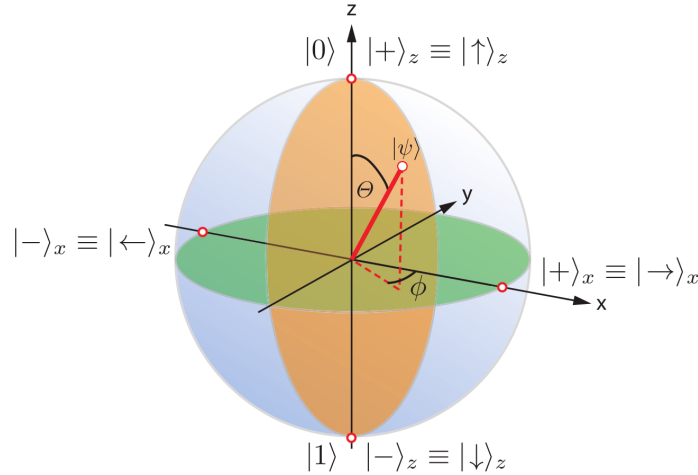
Figure 2.1: **Bloch sphere representation of the quantum two level system** The complex coefficients of a two-level quantum state can be interpreted as spherical coordinates. Here the two states introduced in equation 2.1 correspond to the north and south poles of the depicted sphere. In general any pair of orthonormal states can be used to represent the two-level system, which in this picture means any pair of points on opposing sides of the sphere. From [14]

When several two-level systems are combined the number of possible states grows exponentially. This is analogous to the classical bit, but the number of coefficients, used to describe the state of classical bits, rises linearly with the number of bits, while the number of coefficients for the qubits rises exponentially.

$$|\Psi\rangle_2 = c_{00} |00\rangle + c_{01} |01\rangle + c_{10} |10\rangle + c_{11} |11\rangle \tag{2.3}$$

This property at the same time makes the classical computation of quantum mechanical systems very challenging but also provides new possibilities for computational approaches.

2.2   Trapped Ions as Qubits

The key to utilizing quantum mechanics for computational purposes is to find a system, which can be controlled well enough. To quantify this notion David DiVincenzo formulated five criteria [3]:

1. A scalable physical system with well characterized qubits

2. The ability to initialize the state of the qubits to a simple fiducial state

3. Long relevant decoherence times, much longer than the gate operation time

4. A universal set of quantum gates

5. A qubit-specific measurement capability

A very successful approach to fulfilling these criteria are cold trapped ions. In the implementation considered here $^{40}\text{Ca}^+$-ions are trapped in a linear Paul trap, which is depicted in figure 2.2. Unfortunately it is not possible to trap charged particles in three dimensions using only static electric fields. The solution in the Paul trap is to apply AC voltages along two axes. In this trap the blades, which form an x-shape in the direction transversal to the image plane, form a quadrupole field, by applying an equal voltage to one pair of opposing blades, while applying a voltage of same magnitude but opposing sign to the other pair of blades. This kind of potential would confine a particle along one of the transversal directions, while anti-trapping it along the other. Therefore the voltages on the blades change their signs with frequencies in the radio frequency range. In combination with constant (DC) voltages applied to the tips, which repel the particles along the axis perpendicular to the quadrupole potential, an effective three dimensional trapping of charged particles can be achieved. Through these voltages the trapped ions experience an effective harmonic trapping potential. This approximation holds better, the more the ions sit in the center of the potential, viz. the saddle point of the quadrupole potential. The trap geometry was chosen such, that the trapping potential is elongated along the axis between the DC tips. This results in a trapping situation, where the
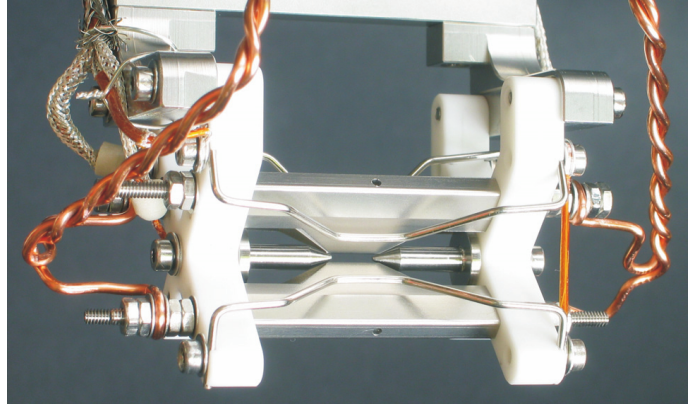
Figure 2.2: **Picture of the linear Paul trap, similar to the one used in the quantum simulation experiment in Innsbruck** This device traps charged particles in a string along the horizontal axis. To do so, the two pairs of blades, two of which are visible in this picture, create an electrical quadrupole field, which alternates at radio frequencies and create an effective harmonic potential perpendicular the string. To confine the particles along the direction of the string the two tips, visible in the picture are set to a constant voltage, which repels the particles.

state of lowest energy for N ions is a linear string along the axis of weakest confinement, instead of a spherical or other geometry. (Fig. 2.3)
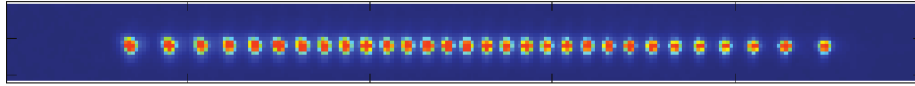
Figure 2.3: **A string of trapped calcium ions** Due to their Coulomb repulsion and the trap geometry ions will arrange in a string, since the confinement along one axis is significantly lower compared to the other two axes. Here a string of 30 ions, with an overall length of 120μm is shown.

2.3 Laser-Ion Interaction

Trapped ions are fairly easy to manipulate, since they can be localized to well below one micron by laser cooling techniques. In the experiment considered here the singly positively charged ions of the calcium isotope ^{40}Ca are trapped. Since calcium has two electrons in its outermost shell the singly charged ion ^{40}Ca$^+$ will exhibit a level structure similar to that of the hydrogen atom. Figure 2.4 shows a simplified scheme of the first few levels of the ^{40}Ca$^+$ ion without the Zeeman structure. The most notable difference to the hydrogen energy levels is the existence of metastable states, $D_{3/2}$ and $D_{5/2}$ with a lifetime of

Figure 2.4: **Simplified level-scheme of** $^{40}\text{Ca}^+$ The qubit is encoded into the $S_{1/2} \to D_{5/2}$ transition, which has a natural lifetim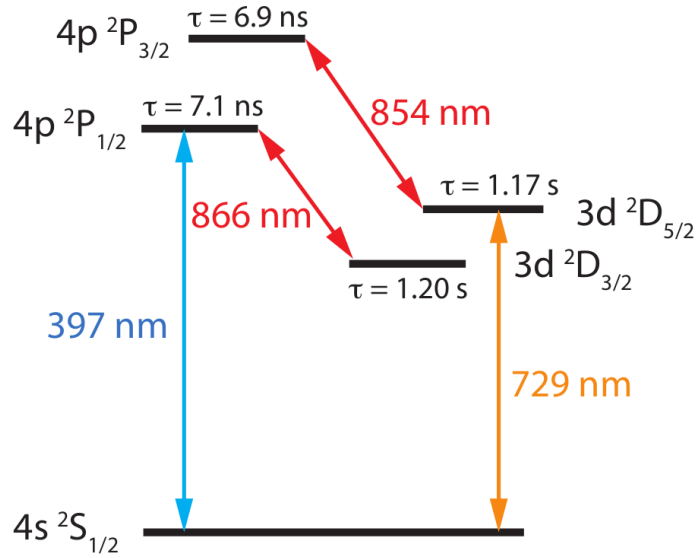e of about 1,17s. The transitions at 397nm, 866nm and 854nm are used for cooling the ions, repumping them to the electronic ground state and readout techniques. From [14]

about 1s. The $S_{1/2}$ and $D_{5/2}$ states are used to encode the qubit and it can be manipulated with light of about 729nm wavelength. This transition is chosen because of its long natural lifetime of 1.17s. This long lifetime is the reason why a laser at 854nm wavelength is needed. It connects the $D_{5/2}$ state to the much more rapidly decaying $P_{3/2}$ state, which allows fast repumping of the electron population to the $S_{1/2}$ state. To detect the state of an ion the transition at 397nm is used. Light of this wavelength is scattered off the ion if it is in the S state and it remains dark if it is in the D state and the scattered light is detected with a photomultiplier tube or a CCD camera. Both P states decay to the S state with probabilities over 90%, nevertheless some population will decay into the D states, which is why a laser at 866nm is needed to pump populations from the $D_{3/2}$ back to the $S_{1/2}$ state. Encoding a qubit in a two-level system, whose transition is driven by frequencies in the optical range is called an optical qubit. An alternative, which does not exist for $^{40}\text{Ca}^+$ would be a hyperfine qubit, which is encoded in two hyperfine sub-levels of one level. The transitions at 397nm and 729nm are also used to cool the motional state of an ion. The 397nm light is used for Doppler cooling, while the 729nm laser is used for sideband cooling, which enables the preparation of the ions in the motional ground state.

The interaction between individual atoms and lasers is typically described in a semi-classical treatment, with a quantized atom and a classical electrical field. A more detailed introduction of this model is given in appendix A. Starting

with the Hamiltonian

$$H = H_0 + H_I \tag{2.4}$$

and the ansatz for the wave function of the electron in the atom

$$|\Psi\rangle = c_1 |1\rangle \, e^{-i\omega_1 t} + c_2 |2\rangle \, e^{-i\omega_2 t} \tag{2.5}$$

a simple equation for the evolution of the states under the influence of the light is obtained:

$$|c_2(t)|^2 = \sin^2\left(\frac{\Omega t}{2}\right) \tag{2.6}$$

Here H_0 is the Hamiltonian of the unperturbed atom, with $|1\rangle$ and $|2\rangle$ its eigenstates. Ω is the so called Rabi frequency, which characterizes the strength of the coupling between the two levels via the light field.

If the atom is illuminated with a pulse of light of duration, such that $\Omega t = \pi$ it follows from this equation, that all population of an atom initially in the state $|1\rangle$ is transferred to the state $|2\rangle$. This is called a π-*pulse* The same holds for the opposite direction, which can be seen in the discussion in the appendix.

Manipulation tools like the π-pulse are the fundamental building blocks to utilize trapped ions for quantum information purposes and fulfill the fourth DiVincenzo criterion. To completely realize a universal set of quantum gates however, another ingredient is essential.

Up to this point only the interaction between a single ion and a light field has been considered. The maybe most important quantum mechanical effect for all quantum information purposes however is the concept of entanglement, which of course only occurs between multiple qubits. This spooky action at a distance, as it was famously called by Einstein, Podolsky and Rosen in 1935 [4], here discussed for two qubits is the notion of non classical correlation. In the quantum mechanical formalism it appears as inability of writing a two particle state as the product of single particle states:

$$|\Psi_{AB}\rangle \neq |\Psi_a\rangle \otimes |\Psi_b\rangle \tag{2.7}$$

An example state for this concept is one of the so called Bell states:

$$\left|\Phi^+\right\rangle = \frac{1}{\sqrt{2}} \left(|\uparrow\uparrow\rangle + |\downarrow\downarrow\rangle\right) \tag{2.8}$$

In our experiments such states are prepared via a multi qubit gate, called the Mølmer-Sørensen gate, which utilizes the common motional modes of the ions to create state dependent optical forces, which mediate entanglement between the electronic states of the ions, in the trap [21].

For these interactions it is necessary, to illuminate all participating ions simultaneously. Even if all parameters in the trap are the same for all ions in the string the Rabi frequency and accordingly the time needed to perform π and $\pi/2$-pulses is directly proportional to the amplitude of the laser at the location of the ion. (cf. equation A.10).

If we wanted to achieve at most 1% of amplitude drop between the most and

least illuminated parts of an ion string, a laser beam's intensity should drop by 1.99% over the length of the string. Assuming a Gaussian intensity profile of

$$I\left(r\right) = I_0 \left(\frac{\omega_0}{\omega}\right)^2 e^{-\frac{2r^2}{w^2}} \tag{2.9}$$

yields an intensity drop by 1.99% at a radius of $r = 0.066w$. For an ion string of 120μm length, the respective r would be 60μm and accordingly $w = 909\mu$m. The fractional intensity inside a certain interval of a Gaussian distribution is given by the error function:

$$I_z = \mathrm{erf}\left(\frac{z}{\sqrt{2}}\right) \tag{2.10}$$

It follows that 5.3% of the total intensity of a Gaussian beam lie within the $0.066w$ interval, required above. So almost 95% of the light are wasted to both sides of the illuminated string. And this fraction only holds under the assumption, that no light is lost above and below the string of ions!

In the following chapters the problem of shaping laser beams to facilitate the desired interaction will be addressed and a device to improve on already implemented technologies is introduced.

Chapter 3

Diffraction, Fourier optics and Holography

In the previous chapter the interaction between light and ions was introduced. During this discussion the light was assumed to be made up of plane waves. However, in a practical implementation this is usually only approximately the case and often not at all. Especially when considering the cost of modern laser systems it is very undesirable to use plane waves of large extent, when they are not needed.

3.1   A scalar theory of diffraction

This chapter is adapted from [10] unless otherwise stated. The central part of Fourier optics and thereby for this thesis is a lens' property to perform a Fourier transformation on a light field that propagates through it. This provides a convenient tool for tasks such as spatial filtering, where the quality of a Gaussian beam can be improved by blocking out features in the frequency domain as well as spatial light modulation. In the latter case an amplitude or phase pattern is imprinted onto a plane wave, chosen such, that the Fourier transform, performed by a lens yields a desired beam shape, such as top-hats or more complex shapes like Bessel beams. The effect goes well beyond geometrical optics and therefore a treatment of lenses in the formalism of diffraction is necessary. First an introduction to the theory of diffraction is given and special care is devoted to the derivation of effects of lenses in different setups.

Maxwell's equations describe classical electrodynamics and with it optics at the most fundamental level, which makes them the usual starting point in textbooks and theses. So let us start from the equations for electromagnetic phenomena:

$$\nabla \times \vec{E} = -\mu \frac{\partial \vec{H}}{\partial t}$$

$$\nabla \times \vec{H} = \epsilon \frac{\partial \vec{E}}{\partial t}$$

$$\nabla \cdot \epsilon \vec{E} = 0$$

$$\nabla \cdot \mu \vec{H} = 0$$

Here $\vec{E}$ and $\vec{H}$ are the electric and magnetic field in vectorial notation respectively. μ and ϵ are the permeability and permittivity of the medium in question. These equations apply for the case of no present free charges. The first step will be to reduce the problem to a scalar one through appropriate approximations. Defining the index of refraction

$$n = \left(\frac{\epsilon}{\epsilon_0}\right)^{1/2}$$

and the vacuum speed of light

$$c = \frac{1}{\sqrt{\mu_0 \epsilon_0}}$$

where μ_0 and ϵ_0 are the permeability and permittivity of the vacuum, the operation $\nabla \times$ can be applied to the first and third equation. With use of the vector identity $\nabla \times \left(\nabla \times \vec{E}\right) = \nabla \left(\nabla \cdot \vec{E}\right) - \nabla^2 \vec{E}$ six independent differential equations are obtained. Therefore the following steps can be performed on one equation of the form

$$\nabla^2 u\left(P, t\right) - \frac{n^2}{c^2} \frac{\partial^2 u\left(P, t\right)}{\partial t^2} = 0 \tag{3.1}$$

where u stands for all $\vec{E}$ and $\vec{H}$ fields' components and P are the spatial coordinates. If only monochromatic waves are considered, which is sufficient in the scope of this thesis, the optical wave can explicitly be written down as:

$$u\left(P, t\right) = \text{Re}\{U\left(P\right)\exp\left(-2i\pi\nu t\right)\} \tag{3.2}$$

where Re{} signifies the real part of what is inside the brackets and $U(P)$ is a complex function called phasor.

$$U\left(P\right) = A\left(P\right)\exp\left[-i\phi\left(P\right)\right] \tag{3.3}$$

Hereby the spatial and temporal dependencies of the optical wave have been separated and the focus can be put on the spatial propagation and transverse effects without having to carry the temporal dependency through the whole calculation. Also the aforementioned simplification of the vectorial nature of electromagnetic waves into a scalar theory was performed. This however is only valid in cases, where the fields' components are independent of each other. This assumption can be made, as long as the structures with which the light interacts are large, compared to the light's wavelength.
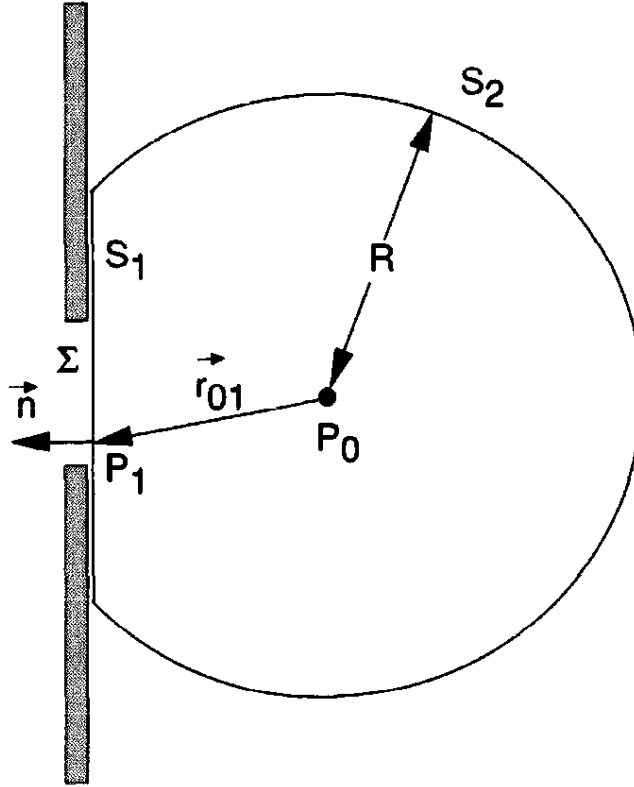
Figure 3.1: **Describing diffraction with Green's functions** To obtain the field at P_0 the field in a volume around it needs to be considered. With Green's functions this can be reduced to considering the surface $S_1 + S_2$ of this volume. In further steps the surface S_2 will be neglected, since no light is incident on P_0 from there. From [10]

Until now only the free propagation of the light wave has been considered. To take into account the interaction between the light and a diffracting aperture consider the situation of figure 3.1. Here a monochromatic plane wave is incident perpendicularly on the screen from the left. Seeking the resulting field at the observation point P_0 the influence of the light diffracted by every point P_1 in the aperture Σ needs to be calculated. In general it would be necessary to calculate the influence of all the light within a volume around P_0, however according to *Green's theorem* [11], this can be reduced to calculating the influence from a surface around P_0. Then the field at position P_0 is given by:

$$U\left(P_0\right) = \frac{1}{4\pi} \iint_{S_1+S_2} \left(G\frac{\partial U}{\partial n} - U\frac{\partial G}{\partial n}\right) ds \qquad (3.4)$$

G is a so called Green's function that can be chosen arbitrarily, within two constraints. G and its first and second partial derivatives need to be single valued and continuous. If it is chosen in a smart way the integration can be simplified significantly. For example it would be desirable to discard the integration over S_2 since it is intuitively clear that, since no light is coming from there, this surface should not contribute to the integration. Let G be

$$G_- (P_1) = \frac{\exp{(ikr_{01})}}{r_{01}} - \frac{\exp{(ik\tilde{r}_{01})}}{\tilde{r}_{01}} \tag{3.5}$$

where r_{01} is the length of the vector that points from the observation point P_0 to the point P_1 within the aperture and $\tilde{r}_{01}$ is the length of the vector pointing from P_1 to a mirror image of P_0, mirrored by the diffracting screen. The quantity k is called wave number and is defined as $k = \frac{2\pi}{\lambda}$. Under the assumption, that the field and its derivative within the aperture Σ are exactly the same as they would be the without the presence of the screen, and the field and its derivatives are exactly zero outside of Σ the integration can be limited even to the transparent part of the screen. This holds for an opaque screen everywhere far (compared to the wavelength λ of the light) from the border between the opaque and transparent regions. If Σ is large compared to λ the evanescent waves, which appear at the border and extend a few wavelengths into the opaque region, can be neglected.
This is the so called first Rayleigh-Sommerfeld solution to the diffraction problem. Simpler functions can be chosen for G, for example the Kirchhoff solution, which is roughly the first term of the Rayleigh-Sommerfeld solution, but additional boundary conditions need to be imposed here, which make the theory inconsistent.
Substituting G_- in 3.4 leads to

$$U(P_0) = \frac{1}{i\lambda} \iint\limits_{\Sigma} U(P_1) \frac{\exp{(ikr_{01})}}{r_{01}} \cos\theta ds \tag{3.6}$$

where θ is the angle between the vectors $\vec{n}$ and $\vec{r}_{01}$. This can be interpreted as the Huygens-Fresnel principle, which says that the field at P_0 can be seen as originating from secondary point sources with diverging spherical waves at each point P_1 within Σ.
This formula allows the calculation of the electromagnetic fields of a diffracted wave in its most general form. In the following approximations will be introduced that radically simplify the calculation of the spatial distribution of light after diffraction.

3.2 Fresnel and Fraunhofer diffraction

Figure 3.2 is a three dimensional extension of figure 3.1, where the direction transversal to the light's propagation has been extended to two dimensions. For

the first approximation the assumption is made, that the distance z, from the aperture plane to the observation plane is much larger, than the spatial extent of the diffracting aperture Σ. In this case $\cos\theta \simeq 1$ and the denominator $r_{01} \approx z$, yielding

$$U(P_0) = \frac{1}{i\lambda z} \iint\limits_{\Sigma} U(P_1) \exp(ikr_{01}) \, ds \qquad (3.7)$$

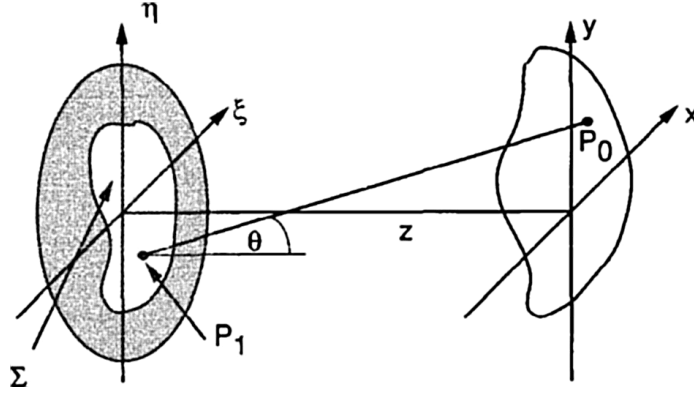To further simplify the expression an assumption for r_{01} in the exponent is

Figure 3.2: **Extended scheme of diffraction geometry.** Light is incident from the left onto the aperture plane, with transversal coordinates (η, ξ) and is diffracted there. At a distance z is the observation plane with transversal coordinates (x,y), containing the observation point P_0. From [10]

made. r_{01} is given exactly by

$$r_{01} = \sqrt{z^2 + (x-\xi)^2 + (y-\eta)^2} = z\sqrt{1 + \left(\frac{x-\xi}{z}\right)^2 + \left(\frac{y+\eta}{z}\right)^2} \qquad (3.8)$$

which can be simplified using the Taylor expansion

$$\sqrt{1+b} = 1 + \frac{1}{2}b - \frac{1}{8}b^2 + \dots \quad |b| < 1 \qquad (3.9)$$

Keeping only the first two terms of the expansion yields

$$z\sqrt{1 + \left(\frac{x-\xi}{z}\right)^2 + \left(\frac{y-\eta}{z}\right)^2} \simeq z\left[1 + \frac{1}{2}\left(\frac{x-\xi}{z}\right)^2 + \frac{1}{2}\left(\frac{y-\eta}{z}\right)^2\right] \qquad (3.10)$$

An assumption on the two terms in brackets needs to be made in order to secure small enough influence of the dropped terms in the expansion. One could impose the condition, that the $b^2/8$-term does not change the phase of the exponential by more than one radian. To meet this condition the following must hold:

$$z^3 \gg \frac{\pi}{4\lambda}\left[(x-\xi)^2 + (y-\eta)^2\right]^2_{max} \qquad (3.11)$$

16

For a circular aperture of 1cm diameter, an observation region of 1cm diameter and a wavelength of 500nm this would mean $z \gg 25cm$.

Inserting equation 3.10 to equation 3.7 ultimately yields:

$$U(x,y) = \frac{e^{ikz}}{i\lambda z} \iint\limits_{-\infty}^{\infty} U(\xi,\eta) \exp\left\{ i\frac{k}{2z} \left[(x-\xi)^2 + (y-\eta)^2 \right] \right\} d\xi d\eta \qquad (3.12)$$

An alternative form is found if the term $\exp \frac{ik}{2z} \left(x^2 + y^2 \right)^2$ is factored outside the integral, yielding

$$U(x,y) = \frac{e^{ikz}}{i\lambda z} e^{\frac{ik}{2z}\left(x^2+y^2\right)} \iint\limits_{-\infty}^{\infty} \left\{ U(\xi,\eta) e^{\frac{ik}{2z}\left(\xi^2+\eta^2\right)} \right\} e^{-i\frac{2\pi}{\lambda z}(x\xi+y\eta)} d\xi d\eta \qquad (3.13)$$

which can be identified, apart from the quadratic phase exponential, as the Fourier transformation of the complex field just after the aperture, where the frequencies would be $f_x = x/\lambda z$ and $f_y = y/\lambda z$. This is called *Fresnel approximation* or referred to as the *near field*.

If another, more strict approximation is applied the quadratic phase exponential can be removed. This is the so called *Fraunhofer approximation* or *far field*. The assumption made is

$$z \gg \frac{k\left(\xi^2+\eta^2\right)_{max}}{2} \qquad (3.14)$$

and it yields the equation

$$U(x,y) = \frac{e^{ikz}}{i\lambda z} e^{\frac{ik}{2z}\left(x^2+y^2\right)} \iint\limits_{-\infty}^{\infty} U(\xi,\eta) e^{-i\frac{2\pi}{\lambda z}(x\xi+y\eta)} d\xi d\eta \qquad (3.15)$$

where again $f_x = x/\lambda z$ and $f_y = y/\lambda z$ are the spatial frequencies in the Fourier transform of the light field directly after the aperture.

For example, for a diffracting aperture of 1 cm diameter and light of 500 nm wavelength z would have to satisfy

$$z \gg 300m \qquad (3.16)$$

This condition is rarely satisfied or satisfiable in laboratory conditions, but in the next chapter it will be shown, how the conditions of Fraunhofer diffraction can be realized at much shorter distances through the use of a converging lens.

3.3 Thin lenses

The central component of Fourier optics, which makes its application practical is the lens. A commonly made approximation to real lenses is that of the thin lens. It states, that the propagation of light through the lens can be viewed as

a phase retardation.

One can write this phase retardation as a transformation of the form $U'(x, y) = t(x, y) U(x, y)$ with U' the field directly after the lens and U the field directly before the lens, as shown in figure 3.3. Here the maximum thickness of the
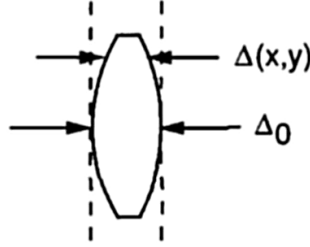

Figure 3.3: **Schematic of a thin lens.** If light propagates through a thin lens the retardation of its phase is directly proportional to the lens' thickness for each ray. Here Δ_0 is the lens' maximum thickness and $\Delta(x, y)$ is the local thickness, depending on the transversal coordinates. From [10]

lens is denoted by Δ_0 and the local thickness, depending on the transversal coordinates by $\Delta(x, y)$. The transformation is then

$$t(x, y) = \exp[ik\Delta_0] \exp[ik(n-1)\Delta(x, y)] \tag{3.17}$$

where n is the refractive index of the lens' material. This can be expressed in words as a global phase retardation due to propagation of the light over the thickness of the lens plus an additional retardation, due to the higher index of refraction of the lens' material and its local thickness.

Before any approximations or simplifications can be made it is helpful to split the thickness function $\Delta(x, y)$ into three parts, as shown in figure 3.4. To parametrize the thickness of the lens it is split into three regions. The left an right curved surfaces and the area of constant thickness between them. Here the maximum thicknesses of the three parts are denoted as Δ_{01}, Δ_{02} and Δ_{03} with $\Delta_0 = \Delta_{01} + \Delta_{02} + \Delta_{03}$. The radii of curvature of the surfaces are chosen such, that with light propagating from left to right, convex surfaces have a positive radius and concave surfaces have a negative one. This allows for the description of several types of lenses, such as biconcave, biconvex, planoconcave and meniscus lenses without changing any formulae. The thicknesses of the curved surfaces are given by

$$\Delta_1(x, y) = \Delta_{01} - R_1 \left(1 - \sqrt{1 - \frac{x^2 + y^2}{R_1^2}}\right) \tag{3.18}$$

and

$$\Delta_3(x, y) = \Delta_{03} + R_2 \left(1 - \sqrt{1 - \frac{x^2 + y^2}{R_2^2}}\right) \tag{3.19}$$
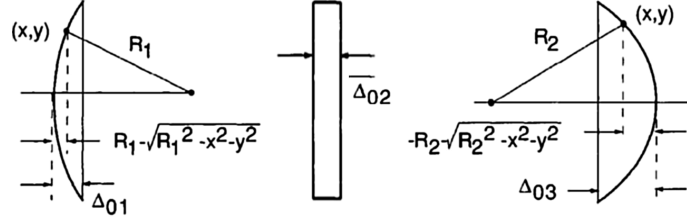
18

Figure 3.4: **Parametrization of the thickness of a lens.** The lens is split into three parts, the left and right curved surfaces and the volume of constant thickness between them. Δ_{01} trough Δ_{03} are the maximal thicknesses of each of the three parts. As a convention the radii of curvature are chosen as follows. With light propagating through the lens from the left to the right convex surfaces (R_1) have a positive radius of curvature, while concave surfaces (R_2) have a negative radius. Adapted from [10]

Joining the three parts and identifying $\Delta_0 = \Delta_{01} + \Delta_{02} + \Delta_{03}$ yields

$$\Delta (x, y) = \Delta_0 - R_1 \left(1 - \sqrt{1 - \frac{x^2 + y^2}{R_1^2}} \right) + R_2 \left(1 - \sqrt{1 - \frac{x^2 + y^2}{R_2^2}} \right) \quad (3.20)$$

Δ_{02} is just a constant term originating from the region of constant thickness of the lens.

To simplify this parametrization an approximation known from geometrical optics is applied. In the so called *paraxial approximation* only light is considered, which propagates approximately through the center of the lens, that is with small x and y coordinates. Then the square root can be simplified using the series expansion of equation 3.9.

$$\sqrt{1 - \frac{x^2 + y^2}{R_i^2}} \approx 1 - \frac{x^2 + y^2}{R_i^2} \quad (3.21)$$

Using the simplified terms in equation 3.20 leads to

$$\Delta (x, y) = \Delta_0 - \frac{x^2 + y^2}{2} \left(\frac{1}{R_1} - \frac{1}{R_2} \right) \quad (3.22)$$

Now the transformation t takes the following form

$$t (x, y) = \exp \left[ikn\Delta_0 \right] \exp \left[-ik (n - 1) \frac{x^2 + y^2}{2} \left(\frac{1}{R_1} - \frac{1}{R_2} \right) \right] \quad (3.23)$$

Additionally all physical properties of the lens can be combined into one quantity f, which is defined by

$$\frac{1}{f} = (n - 1) \left(\frac{1}{R_1} - \frac{1}{R_2} \right) \quad (3.24)$$

called the *focal length* of the lens. Substituting the focal length and dropping the constant phase retardation in the above equation now yields

$$t\left(x,y\right)=\exp\left[-i\frac{k}{2f}\left(x^2+y^2\right)\right] \tag{3.25}$$

This equation approximates the effect of a spherical lens by parabolic surfaces for the case of paraxial illumination. In the non-paraxial case the behavior of the lens will differ significantly from this approximation and the differences are quantified and discussed in the context of aberrations in section 5.3.

As stated above the sign convention for the radii of curvature of the spherical surfaces allows the description of different types of lenses and it can be shown, that equation 3.25 yields meaningful results in all cases with the sign of f indicating the type of lens. $f > 0$ means that the focal point of the lens is at a distance f behind it and a plane wave is turned into a spherical wave converging on the focal point. That is the case for biconvex, planoconvex and positive meniscus lenses. These are therefore called *positive* or *converging* lenses. $f < 0$ describes lenses with a focal point behind the lens, meaning that a plane wave would be turned into a spherical wave, appearing to diverge from the focal point in front of the lens. These lenses are biconcave, planoconcave or negative meniscus lenses. They are called *negative* or *diverging* lenses and are depicted in figure 3.5.
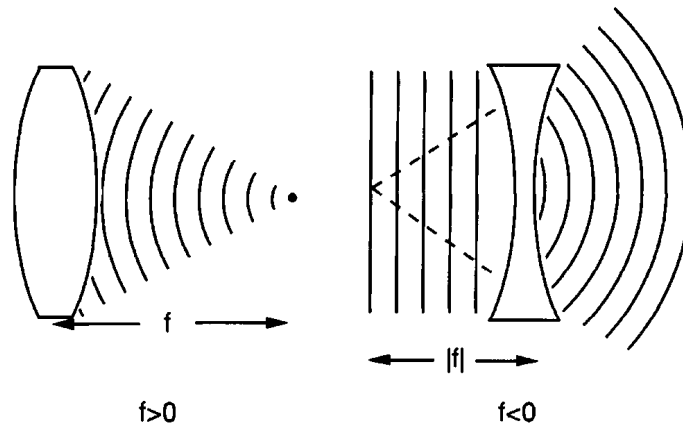

Figure 3.5: **Two types of lenses.** Lenses with $f > 0$ are called converging lenses, since a plane wave incident onto the lens converges onto a point after the lens. Lenses with $f < 0$ are called diverging lenses, because a plane wave diverges, after propagating through the lens. From [10]

3.4 Fourier transforms with lenses

As mentioned above thin lenses can be used to perform Fourier transforms, as in the Fraunhofer approximation of diffraction, without having to observe the diffracted field at distances of the order of 1000 m. To show this property two different setups shall be discussed, as shown in figure 3.6.
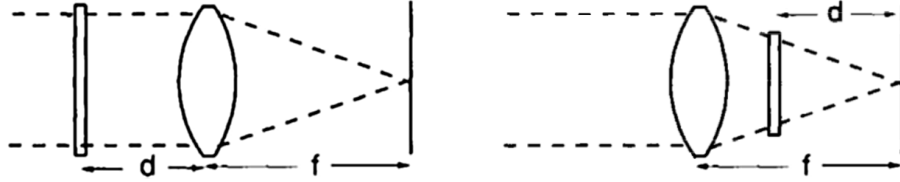

Figure 3.6: **Setups to perform Fourier transformations with lenses.** On the left the aperture is placed at a distance d in front of the lens. On the right the aperture is placed behind the lens, a distance d from the focal plane of the lens. The latter case is equivalent to illuminating the aperture with a spherical wave. From [10]

Aperture before the lens

The first setup to be discussed is shown on the left side of figure 3.6. The aperture is placed a distance d in front of a converging lens and the observation plane is the focal plane of said lens. Here the angular spectrum of the wave will be considered, which is defined as

$$F_U\left(f_x, f_y\right) = \mathcal{F}\{U\} = \iint\limits_{-\infty}^{\infty} U\left(x, y\right) \exp\left[-2\pi i\left(f_x x + f_y y\right)\right] dx\ dy \qquad (3.26)$$

It is assumed that the aperture is illuminated by a plane wave of amplitude A and has a complex transformation function $t_0\left(x, y\right)$, which can be a simple binary function, with value 1 inside the aperture and 0 outside it or something more complicated with phase delays and amplitude modulations, depending on the transversal coordinates. The spectrum of the light At_0 directly after the aperture is $F_0 = \mathcal{F}\left[At_0\right]$ and the spectrum of the light U_l directly in front of the lens is $F_l = \mathcal{F}\left[U_l\right]$. This angular spectrum can be interpreted as plane waves propagating in different directions and interfering to make up the field in real space.
The spectra directly behind the aperture and directly behind the lens can be related by an equation that holds in the case of Fresnel diffraction

$$F_l\left(f_x, f_y\right) = F_0\left(f_x, f_y\right) \exp\left[-i\pi\lambda d\left(f_x^2 + f_y^2\right)\right] \qquad (3.27)$$

where d is the distance between the aperture and the lens. This follows from equation 3.12, which can be viewed as a convolution of U with the kernel

$h(x, y) = \frac{e^{ikz}}{i\lambda z} \exp\left[\frac{ik}{2z}(x^2 + y^2)\right]$. For the spectra the convolution turns into a product as in equation 3.27, where the transformed kernel is

$$H(f_y, f_y) = e^{ikz} \exp\left[-i\pi\lambda z\left(f_x^2 + f_y^2\right)\right] = \mathcal{F}\{h(x,y)\} \qquad (3.28)$$

This can be interpreted as an additional phase, collected by the different spatial frequencies originating from their different directions and thereby different path lengths. Considering again the equation for Fresnel diffraction

$$U_z(x, y) = \frac{e^{ikz}}{i\lambda z} e^{\frac{ik}{2z}(x^2+y^2)} \iint\limits_{-\infty}^{\infty} \left\{ U(\xi, \eta) e^{\frac{ik}{2z}(\xi^2+\eta^2)} \right\} e^{-i\frac{2\pi}{\lambda z}(x\xi+y\eta)} d\xi d\eta \quad (3.29)$$

helpful observations can be made. Since the observation plane is the focal plane of the lens, z is set equal to the focal length f. Now the exponential e^{ikf} in front of the integral can be dropped, since it is a global phase. Setting $U(\xi, \eta)$ according to the preceding chapter

$$U_l(\xi, \eta) = At_0(\xi, \eta) \exp\left[-i\frac{k}{2f}(\xi^2 + \eta^2)\right] \qquad (3.30)$$

where t_0 is again an arbitrary complex function, that contains the modifications to the amplitude of the field and A is the amplitude of the plane wave. Now the two exponentials depending on ξ and η cancel and the field U_f at the plane $z = f$ is

$$U_f(x, y) = \frac{\exp\left[\frac{ik}{2f}(x^2 + y^2)\right]}{i\lambda f} \iint\limits_{-\infty}^{\infty} At_0(\xi, \eta) \exp\left[-i\frac{2\pi}{\lambda f}(x\xi + y\eta)\right] dx dy$$
$$(3.31)$$

Identifying $f_x = \xi/\lambda f$ and $f_y = \eta/\lambda f$ allows substitution of the angular frequency spectrum, yielding

$$U_f(x, y) = \frac{\exp\left[\frac{ik}{2f}(x^2 + y^2)\right]}{i\lambda f} F_l\left(\frac{x}{\lambda f}, \frac{y}{\lambda f}\right) \qquad (3.32)$$

As the last step equation 3.27 is substituted into equation 3.32, yielding

$$U_f(x, y) = \frac{\exp\left[\frac{ik}{2f}(x^2 + y^2)\right]}{i\lambda f} F_0\left(\frac{x}{\lambda f}, \frac{y}{\lambda f}\right)$$
$$= \frac{A\exp\left[\frac{ik}{2f}\left(1 - \frac{d}{f}\right)(x^2 + y^2)\right]}{i\lambda f} \iint\limits_{-\infty}^{\infty} t_0(\xi, \eta) \exp\left[-i\frac{2\pi}{\lambda f}(x\xi + y\eta)\right] d\xi d\eta$$
$$(3.33)$$

Apart from the phase exponential in front of the integral this is the Fourier transform of the field, that propagated from the aperture to the lens. In the special case of $d = f$, meaning the aperture being placed in the front focal plane of the lens, the exponential in front drops out, leaving the *exact* Fourier transform of the light diffracted by the aperture.

Aperture behind the lens

Placing the aperture behind the lens, as is depicted in figure 3.6 on the right is equivalent to illuminating the aperture with a converging spherical wave, if the lens is in turn illuminated by a plane wave of amplitude A. From geometrical optics it follows, that the local amplitude at distance d behind the lens is given by $A\frac{f}{d}$, where d is now the distance of the aperture to the focal plane. That means in the case $d = f$ the aperture would be placed directly against the lens and would be illuminated by the unchanged amplitude, since no focusing has occurred yet. For $d = 0$ the amplitude diverges, since in this approximation of a lens of infinite size the focus spot would be infinitely small.

Using again the formalism from before the light transmitted by the aperture becomes

$$U_0\left(\xi, \eta\right) = \left(\frac{Af}{d} \exp\left[-i\frac{k}{2d}\left(\xi^2 + \eta^2\right)\right]\right) t_0\left(\xi, \eta\right) \tag{3.34}$$

Again substituting this into the equation for Fresnel diffraction yields

$$U_f\left(x, y\right) = \frac{A \exp\left[i\frac{k}{2d}\left(x^2 + y^2\right)\right]}{i\lambda d}\frac{f}{d}\iint\limits_{-\infty}^{\infty} t_0\left(\xi, \eta\right) \exp\left[-i\frac{2\pi}{\lambda d}\left(x\xi + y\eta\right)\right] d\xi d\eta$$

$$\tag{3.35}$$

which is, again up to a quadratic phase factor, the Fourier transform of the transmission function of the aperture. But in this case an additional feature appears. The factor $\frac{f}{d}$ means, that by moving the aperture closer to or farther from the lens the size of the image, formed in the focal plane, can be controlled. It is important to note, that in the above discussion no constraints were put on the aperture function t_0. In general t_0 can be an arbitrary complex-valued function, although in practice a device or optical element taking the role of the aperture will not manipulate both degrees of freedom of an incident wave.

3.5   Aberrations

In the previous section the description of a thin lens was introduced, albeit with a couple of assumptions. Most importantly the spherical surface of the lens was approximated through parabolic functions, which only hold for light propagating through the lens close to the optical axis.

Deviations from the ideal behavior of an optical system are called aberrations. They limit the performance of optical systems, such as telescopes or photographic lenses and great effort is taken to minimize the aberrations of an optical system.

To develop a description of aberrations I will consider the response of an optical system being illuminated by a plane wave. A perfect system would image the plane wave onto a point in the image plane, whose position depends on the plane wave's angle of incidence onto the entrance pupil of the system. The deviation of the image from this ideal point focus is called *point-spread-function*.

An ideally focussed plane wave would leave the optical system as a spherical wavefront, converging on a point in the image plane. Let this spherical wavefront be denoted as S and the actually produced wavefront as W, as depicted in figure 3.7. Let P_1' be the point in the plane of the output pupil from which an imagined ray of light propagates to the image point. Now P_1^* is the point in the image plane, where the image of the plane wave is expected to appear for an ideal optical system. The actual point of convergence for the wavefront after the exit aperture is denoted as P_1. The points Q and Q' are defined as the points, where a ray from P_1 or P_1^* intersects the ideal or actual wavefront, which crosses the center of the pupil.

Now the aberration can be quantified through the optical path length $\Phi = [QQ']$. Instead of continuing the geometrical discussion of the optical aberration, Φ shall now be expanded in a power series.
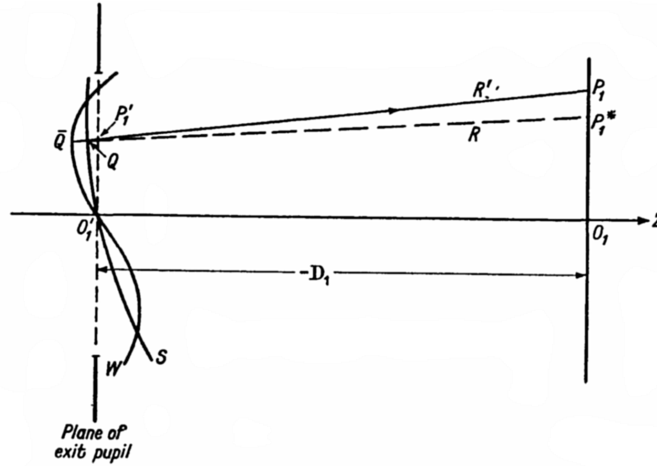

Figure 3.7: **Quantifying the distortion of a wavefront through an optical system** The planes at O_1' and O_1 correspond to the exit pupil of the optical system in question and the image plane respectively. The ideal wavefront S would lead to a focus spot at location P_1^*, while the actual distorted wavefront W produces the focus point at location P_1. The optical path length between S and W, denoted by the points Q and Q' is used to measure the degree of aberration for each point in the exit pupil. The points Q and Q' are defined as points in the wavefronts, which cross the center of the pupil plane, where a ray from P_1 or P_1^* crosses these wavefronts. From [1]

This expansion will be done in terms of the Zernike polynomials $V_n^l(X, Y)$, which in polar coordinates take the form $V_n^l(\rho \sin \theta, \rho \cos \theta) = R_n^l(\rho) e^{il\theta}$. The

radial functions R_n^l are defined by:

$$R_n^{\pm m}(\rho) = \sum_{s=0}^{\frac{n-m}{2}} (-1)^s \frac{(n-s)!}{s!\left(\frac{n+m}{2} - s\right)!\left(\frac{n-m}{2} - s\right)!} \rho^{n-2s} \qquad (3.36)$$

Here $n \geq 0$ and l are integer numbers, with $n \geq |l|$ and $n - |l|$ even, as well as $m = |l|$.

While the polynomials V are complex, real polynomials can be defined, yielding even and odd functions in θ.

$$U_n^m = \frac{1}{2}\left(V_n^m + V_n^{-m}\right) = R_n^m(\rho)\cos m\theta \qquad (3.37)$$

$$U_n^{-m} = \frac{1}{2i}\left(V_n^m - V_n^{-m}\right) = R_n^m(\rho)\sin m\theta \qquad (3.38)$$

The path length difference Φ now becomes

$$\Phi(\rho, \theta) = \sum_n \sum_m a_{nm} R_n^m(\rho)\cos m\theta + a'_{nm} R_n^m(\rho)\sin m\theta \qquad (3.39)$$

The terms of this expansion are well known deformations of optical systems and the lowest of them are listed in table 3.1. Expanding a wavefront in the Zernike polynomials yields a unique set of coefficients, as is shown in [1] and these coefficients can be used to quantify the amount of aberrations in an optical system. Some of the most notable aberrations are:

- *Tilt* is just as the name suggests a tilting of the overall wavefront along an axis.

- *Defocus* is the distortion of a focus due to a shifted image plane.

- *Astigmatism* results, when the optical system has a different focal lengths along two perpendicular axes. That means, that at a certain distance a focus will appear as a line along one of these axes, and at another distance another focus will appear as a line along the other axis.

- *Coma* appears, when the magnification of an optical system varies with the position inside the pupil. It leads to a distorted focus with the shape of a comet's tail.

- *Spherical aberration* is a varying focal length, depending on the position within the optical system's pupil.

Aberrations can severely limit the performance of optical systems and a part of this thesis will be to explore the capabilities of a spatial light modulator to correct for the aberrations in an optical setup. Section 5.3 describes the optical setup that was tested and the experimental scheme that was applied to correct for the aberrations present in that system.
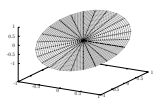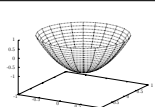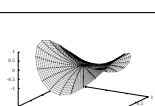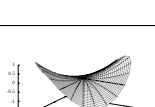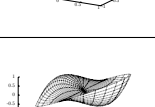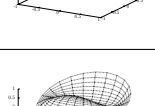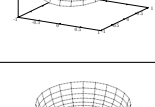
Name	Polynomial	Depiction
Piston	a_0	-
X-tilt	$a_1 * \rho \cos \theta$	
Y-tilt	$a_2 * \rho \sin \theta$	
Defocus	$a_3 * \left(2\rho^2 - 1\right)$	
0° Astigmatism	$a_4 * \rho^2 \cos \left(2\theta\right)$	
45° Astigmatism	$a_5 * \rho^2 \sin \left(2\theta\right)$	
X-coma	$a_6 * \left(3\rho^2 - 2\right) \rho \cos \theta$	
Y-coma	$a_7 * \left(3\rho^2 - 2\right) \rho \sin \theta$	
Spherical	$a_8 * \left(6\rho^4 - 6\rho^2 + 1\right)$	

Table 3.1: **Some of the most notable Zernike polynomials** Using the coefficients a_0 to a_n a distorted wavefront can be quantitatively analyzed and the aberrations can be corrected for accordingly. There is no image for the polynomial "piston" since it only corresponds to a constant phase shift of the wavefront, without any features in need of depiction.

3.6 Holography

The first thing that comes to mind when thinking of apertures are simple geometrical forms like rectangles and circular apertures. However, these are only of scientific interest in the context of resolution of optical systems or for educational purposes, since their diffraction patterns are relatively easy to calculate. Transparencies with absorptive structures and modern electro optical devices allow the construction of far more complex apertures, which are capable of creating arbitrary light patterns and are limited only by technology. These apertures are called holograms.

Classical holograms

Typically holography, as Dennis Gabor envisioned it [8], is a technique to record the amplitude and phase of light, that gets scattered off an object, as opposed to photography, which is only sensitive to the intensity of the scattered light. To do so the same detectors as for photography can be employed, but the phase differences need to be turned into amplitude differences through interferometry. The light to be recorded is overlapped with light from another source with known relative phase, e.g a plane wave. The recorded image is then converted into a transparency, where the recorded intensities are turned into transmittivities. (cf. figure 3.8) Let $\mathbf{a}(x,y) = a(x,y)\exp\left[-i\phi(x,y)\right]$ and
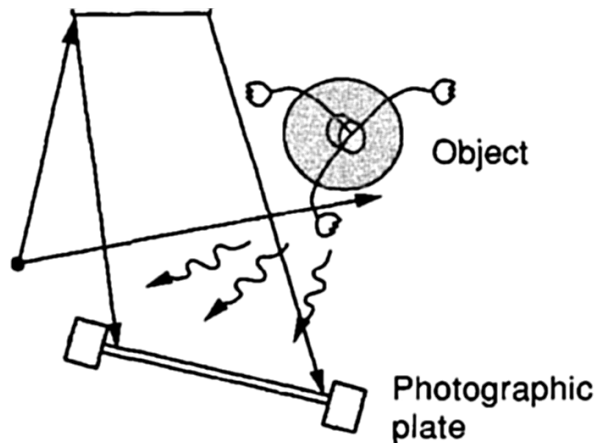
Figure 3.8: **Example of a hologram recording scheme.** A hologram is created through the interference of the light scattered off the object to be recorded and light from a reference source. In the case depicted here the reference is created by reflecting part of the incident light off a mirror and overlapping the reflected light with the scattered at the recording medium. From [10]

$\mathbf{A}(x,y) = A(x,y)\exp\left[-i\psi(x,y)\right]$ be the wavefronts of the scattered light and

the reference light respectively and let us assume, that the intensity $|\mathbf{A}|^2$ is uniform. Then the intensity of the sum becomes:

$$I\left(x,y\right) = |\mathbf{A}|^2 + |\mathbf{a}\left(x,y\right)|^2 + 2Aa\left(x,y\right)\cos\left[\psi\left(x,y\right) - \phi\left(x,y\right)\right] \qquad (3.40)$$

The resulting intensity contains information about the amplitude and the phase of the scattered light. A transparency recording this intensity is called a hologram. First we assume, that the transparency has high average transmittivity and the recording changes that only by small amounts.

$$\mathbf{t}\left(x,y\right) = t_0 + \Delta t\left(x,y\right) \qquad (3.41)$$

where $|\Delta t| \ll |t_o|$. If we assume the recording medium to be linear, that means, the resulting transmittivity of the, for example, film is directly proportional to the incoming intensity, the transparency takes the form:

$$\mathbf{t}\left(x,y\right) = \beta\left(|\mathbf{A}|^2 + |\mathbf{a}|^2 + \mathbf{A}^*\mathbf{a} + \mathbf{A}\mathbf{a}^*\right) \qquad (3.42)$$

β is a coefficient, characterizing the response of the recording medium. The term $\beta|\mathbf{A}|^2 = \mathbf{t}_b$ creates a constant transmittivity, which will be called bias and which also includes the transmitted light from the t_0 term. To reconstruct the wavefront this transparency is now illuminated with a new coherent wave $\mathbf{B}\left(x,y\right)$.

$$\mathbf{B}\left(x,y\right)\mathbf{t}_f\left(x,y\right) = \mathbf{t}_b\mathbf{B} + \beta\mathbf{a}\mathbf{a}^*\mathbf{B} + \beta\mathbf{A}^*\mathbf{B}\mathbf{a} + \beta\mathbf{A}\mathbf{B}\mathbf{a}^* \qquad (3.43)$$
$$= \mathbf{U}_1 + \mathbf{U}_2 + \mathbf{U}_3 + \mathbf{U}_4$$

Now, if $\mathbf{B}$ is exactly equal to $\mathbf{A}$ the third term becomes

$$\mathbf{U}_3\left(x,y\right) = \beta|\mathbf{A}|^2\mathbf{a}\left(x,y\right) \qquad (3.44)$$

Since we assumed $|\mathbf{A}|^2$ to be uniform, this term is up to a constant factor a replica of the original wavefront. An observer behind the transparency would therefore detect light, as if it were scattered off the original object, even though it is not present anymore.

Under the assumption of small variations to the transmittivity the term $\mathbf{U}_2$ is negligible. $\mathbf{U}_4$ is proportional to $\mathbf{a}^*$ and therefore yields the conjugate of the object wave.

In other words the reconstruction process will yield a virtual image of the object in front of the screen, the original wave, and a real image, behind the screen, the conjugate wave. The real and virtual image will appear at locations, which are mirror images of each other, from the hologram transparency. This means, that by recording the hologram with an angle between the object and the reference wave, will separate these two images automatically.

A point, that will be important in the following section is, that for these techniques the object whose wave is to be recorded needs to be present in the recording apparatus at some point and therefore needs to exist.

Computer generated holograms

Thanks to the high computational power of modern computers a new field of holography has emerged. Through specialized algorithms it has become possible to *calculate* the structure of transparencies for a given object. In turn this means that in contrast to the techniques presented above, the object, whose light field is to be reconstructed, need not have existed at any point in time!
While it is possible to calculate holograms, that form three dimensional images, this thesis will focus on a technique to create a two dimensional image, simply because depth information is not of interest in our application. Holograms which are calculated, instead of recorded are called *computer generated holograms*, or CGH and the type of CGH considered here is of the Fourier hologram type, because it employs the Fourier transforming properties of lenses. Two kinds of Fourier holograms can be distinguished: Amplitude holograms encode the information into the amplitude of the transparency, similar to classical holography. On the other hand phase holograms assume a transparency of uniform transmittivity but encode the image into relative phase shifts of the transmitted wavefront. For a comparison of an amplitude and a phase hologram of a simple rectangle, see figure 3.10. It is sufficient to use only one degree of freedom to encode the hologram, since we are only interested in controlling one degree of freedom, namely the amplitude, in the image plane. The value of the phases for the reconstructed image is of no concern, as long as it is fixed.
Since the device used to encode the CGH in this thesis is a phase-only spatial
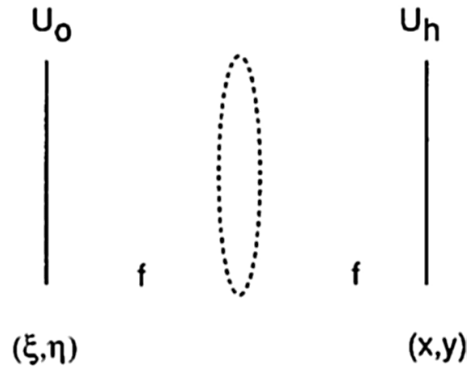
Figure 3.9: **Fourier hologram** A Fourier hologram assumes that the hologram to be calculated (U_h) is the Fourier transform of the light in the object plane(U_o). E.g. the light was imaged through a lens, which is indicated with dotted lines here. In the reconstruction of the object a real lens is used to transform the light from the hologram once more. From [10]

light modulator (cf. section 4.3) the focus will lie on phase holograms in the following.
The creation of a CGH can be split into three problems, sampling, computation and encoding. While the computation problem is addressed in the following

section, the encoding problem is discussed in chapter 4 where liquid crystals as a means of modulating the phase of a light field are discussed and the device used in this thesis is introduced.

The sampling problem is concerned with the necessary sampling distance in the hologram plane, to achieve a desired resolution in the image plane. It is only of minor importance in this thesis, since the sample distance in the hologram plane is fixed through the physical properties of the device that encodes the hologram. However, in reversing the problem, a formula for the size of the reconstructed image can be given:

$$L_\xi = \frac{\lambda f}{\Delta x} \qquad (3.45)$$

Limiting the discussion to one spatial dimension L_ξ is the extent of the reconstructed image in the image plane, f is the focal length of the lens used in the reconstruction, λ is the wavelength of the light used and Δx and is the sample spacing in the hologram plane in the x direction. This formula can be derived with a few simple considerations. The hologram can be seen as a means to diffract light into different directions. If the hologram were chosen as a diffraction grating the maximum deflection of the light can be obtained from the grating equation

$$n\lambda = d \cdot \sin\theta \qquad (3.46)$$

where n is the index of the diffraction maximum, which shall be one here, d is the grating constant, in this case this is $2\Delta x$, which is the finest grating that can be displayed with a sample spacing of Δx and θ is the corresponding angle of deflection. Using a lens to image the deflected light leads to

$$\tan\theta = \frac{L}{f} \qquad (3.47)$$

with L the distance of the deflected light from the optical axis in the image plane and f the focal length of the lens. In the case of small deflection angles the approximations $\tan x = x = \sin x$ can be used to get

$$\lambda = 2\Delta x \cdot \frac{L}{f} \qquad (3.48)$$

Recognizing that the extent of the image L_ξ is twice the deflection distance L equation 3.45 is obtained.

3.7   Algorithms to calculate CGHs

The holograms considered here encode the information in the phase of the light field and are therefore called phase-holograms. The calculation of phase-holograms is significantly more difficult than that of amplitude holograms and it is usually very hard, if not impossible, to infer anything about the image by looking at a phase hologram. In an amplitude hologram the connection between

features of the hologram and features of the image is readily made, since the transverse locations in the hologram plane can be associated with spatial frequencies, which can be identified in the image plane. For example in figure 3.10 the rectangular structure of the input pattern is easily recognized, although its shift from the central position is not obvious even here. In phase-holograms the correspondence between spatial frequencies in the image plane and transverse points in the hologram of course also exists, but since the amplitude of all points in the hologram plane is usually equal no information can be inferred form this. Instead the points in the hologram plane are assigned relative phases. The right side of figure 3.10 shows such a phase hologram. Here the gray levels no longer signify a transmitted amplitude, but rather the relative phases of the light field's components.

The modulated light that propagates from the hologram plane is usually imaged by a positive lens, as shown in the previous chapter. The different components' interference then leads to the formation of the desired pattern in the image plane. Apart from very simple cases, such as diffraction gratings and lenses it is
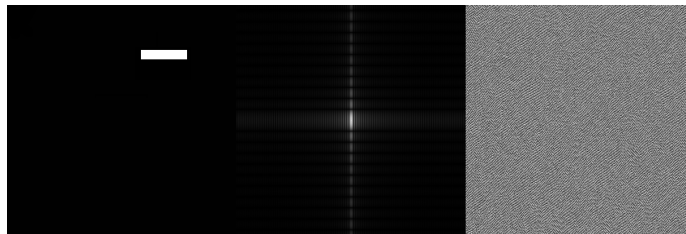
Figure 3.10: **Comparison between an amplitude and a phase hologram** These images show an amplitude hologram in the center and a phase hologram calculated by the GS algorithm on the right. The starting point for the holograms was the shifted rectangle depicted on the left. For the amplitude hologram on the left the contrast was enhanced, to emphasize the spatial components, which allow an identification with the spatial directions of the numeral. Although it is not obvious, that the rectangle in the input image was shifted from the central position, the general shape is quickly recognized. In the phase hologram on the right no such identification is possible, since the gray levels here correspond to relative angles in the interval $[0; 2\pi]$.

usually not possible to predict the image from simply looking at the hologram. The algorithms used to calculate phase holograms can be divided into two families: Point source algorithms [26] and iterative Fourier transform algorithms. Only the latter shall be discussed in this thesis. An iterative Fourier transform algorithm (IFTA), starts with an initial guess of the hologram and approaches a solution, which approximates the desired image to a predefined amount of error. An example of an IFTA is given and a first extension of the algorithm is shown.

3.7.1 Gerchberg-Saxton Algorithm

A very basic algorithm of the iterative transform type is the so called *Gerchberg-Saxton algorithm* [9]. It is schematically depicted in figure 3.11. This algorithm
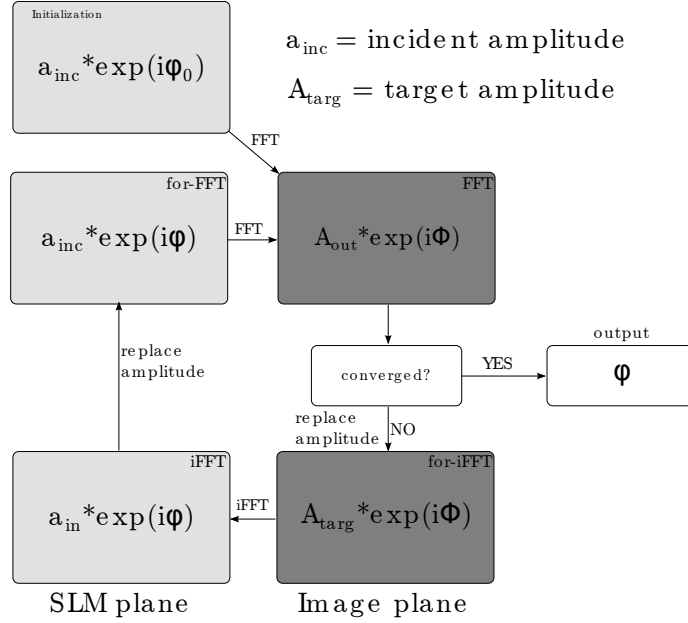

Figure 3.11: **Schematic depiction of the Gerchberg-Saxton algorithm.** To initialize the algorithm the amplitude of the incident light (a_{inc}) and an initial guess for the phases (φ_0) are combined to form a complex field. Through iterative Fourier transformation and application of constraints on the complex field the pattern of phases approaches the solution. If the resulting image (A_{out}) approximates the desired image up to a predefined measure of error the iteration is stopped and the phase pattern is extracted.

is initialized, by creating a complex field from the amplitude of the incident light, (a_{inc}) which is usually chosen to be uniform over the whole hologram, and an initial guess for the phases (φ_0). This field $a_{inc}\exp[i\varphi_0]$ is then Fourier transformed to yield $A_{out}\exp[i\phi]$.

$$A_{out}\exp[i\phi] = \mathcal{F}\left(a_{inc}\exp[i\varphi]\right) \tag{3.49}$$

This is the image plane and A_{out} corresponds to the amplitude of the light field, that would form, if φ were used as an actual hologram. Now the convergence criterion is invoked. For each point in A_{out} the difference from the corresponding point of the desired, or target, image A_{targ} is calculated and the root-mean-squared error is calculated. If this value lies below a preset bound, which is usually chosen to be a few percent, and does not change by a preset amount between two iterations, the algorithm is considered converged and φ is the

desired hologram.

The root mean squared error is given by

$$RMSE = \frac{1}{\sqrt{n}} \sqrt{\sum_{i,j} \left(A_{out}\left(i,j\right) - A_{targ}\left(i,j\right)\right)^2} \tag{3.50}$$

where i and j index the points in the sampled fields and $n = i \cdot j$ is the overall number of samples. To ensure the comparability of both amplitudes they need to be normalized appropriately. If the algorithm is not converged the next step is to replace the amplitude of the output A_{out} with the amplitude corresponding to the target pattern A_{targ}, while the calculated angles are kept.

$$A_{out} \exp\left[i\phi\right] \to A_{targ} \exp\left[i\phi\right] \tag{3.51}$$

In the next step the inverse Fourier transform of the expression above is taken

$$a_{in} \exp\left[i\varphi\right] = \mathcal{F}^{-1}\left(A_{targ} \exp\left[i\phi\right]\right) \tag{3.52}$$

Finally a_{in} is replaced by the incident amplitude a_{inc} and the next iteration begins

$$a_{in} \exp\left[i\varphi\right] \to a_{inc} \exp\left[i\varphi\right] \tag{3.53}$$

In principle the algorithm propagates the field back and forth between the hologram plane and the image plane and uses the amplitude of the incident light and the target image as constraints on the evolution of the phases.

Figure 3.12 shows an example for the GS algorithm. In a) the chosen target can be seen, which was put into the algorithm as A_{targ} and b) shows the output phase pattern, with the brightness values from 0 to 255 translating into a relative phase from 0 to 2π. c) is the reconstructed image, from applying the phase pattern to the SLM and imaging the diffracted light onto a CCD camera. While the general shape of the target pattern is reconstructed fairly well, the homogeneity of the shape however is very poor, due to speckle and imperfect convergence. The first step to improve image quality is given in the following chapter on the MRAF algorithm, and further improvements are discussed in section 5.4. General convergence of this algorithm can only be proven in the weak sense, that means, that from one iteration to the next the error measure, in this case the RMS error can not increase [6]. It is immediately obvious, that this leads to a problem, since the algorithm can never escape from a local minimum of the convergence criterion, should it encounter one.

3.7.2 MRAF

There are different improvements on the Gerchberg-Saxton algorithm, which aim at avoiding getting stuck in local minima of the convergence, one of which will be presented here. The mixed region amplitude freedom (MRAF) algorithm [19] improves on the GS algorithm by relaxing the constraints on the amplitudes in the image plane. This is achieved by splitting the image plane into two parts,
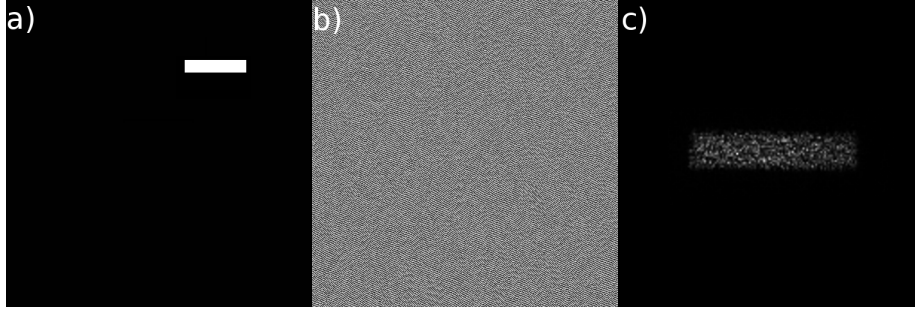
Figure 3.12: **Example images for the GS algorithm:** a) Shows the chosen target pattern, a shifted rectangle. b) Is the pattern that was calculated, using the GS algorithm, c) shows the reconstructed image, when the calculated pattern is applied to the SLM and the diffracted light is imaged with a CCD camera. This image was cropped, to improve visibility. Here it can be seen, that the GS algorithm reconstructs the shape of the target, to a certain amount of precision, but a large amount of speckle remains and reduces the image quality.

a signal region (SR), which contains the desired image and a noise region (NR), where the amplitude is not constrained at all. During the iteration the amplitude A_{out} is replaced by A_{targ} only for the pixels in the signal region, while the evolution of the amplitudes in the noise region is fully unconstrained. In practice that means, that the usable area of the image plane is reduced, compared to the GS algorithm, since the number and size of pixels in the hologram plane are fixed.

Here, equation 3.51 becomes:

$$A_{out} \exp\left[i\phi\right] \to \left(m \cdot A_{targ}|_{SR} + (1-m) \cdot A_{out}|_{NR}\right) \exp\left[i\phi\right] \qquad (3.54)$$

Also the signal and noise region are weighted against each other, using a mixing factor 'm'. While a higher mixing factor reduced the number of iterations until the algorithm converges it also reduces the smoothness of the output. To yield a good balance between these properties the mixing factor was chosen to be 0.3 but lower values can be explored, since fast calculation is not a strict requirement in our implementation.

Apart from the division into two regions the procedure of the MRAF algorithm is the same as for the GS. The noise region can for example be chosen to frame the signal region but in general the relative positioning is arbitrary. Figure 3.13 shows example images for the MRAF algorithm, equal to those of figure 3.12. First the target pattern is shown, as before, the shifted rectangle. Sub-figures b) and c) show the calculated phase pattern, Sub-figure c) shows the image, produced in the focal plane of a positive lens, imaged with a CCD camera. It can be seen, that the quality of the image has improved, compared to the GS algorithm, but to achieve acceptable homogeneity of homogeneous areas, further improvements are necessary. A straightforward way to compare the two
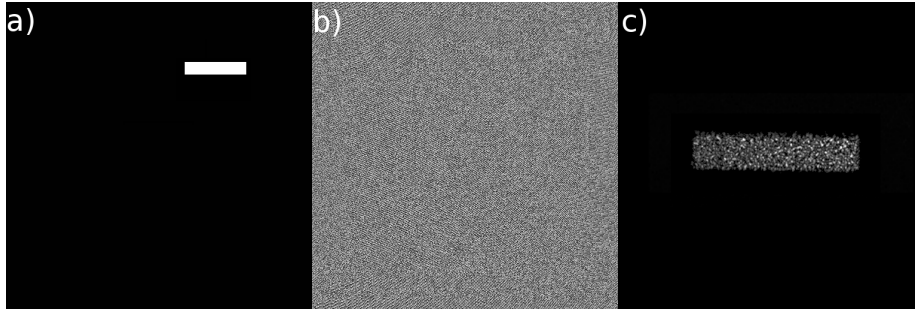
Figure 3.13: **Example images for the MRAF algorithm:** a) Shows the chosen target pattern, a shifted rectangle. b) Is the pattern that was calculated, using the MRAF algorithm, c) shows the reconstructed image, when the calculated pattern is applied to the SLM and the diffracted light is imaged with a CCD camera. Improvement, in comparison with the GS algorithm (cf. figure 3.12 d) can be observed but further tricks and improvements are needed for acceptable image quality

algorithms is to compare their output intensities. These are the "ideal" images, that the algorithms predict, if the implementation of the phase hologram were perfect. In contrast to that, the reconstructed image, or intensity is always what was actually measured in a test setup. The output amplitude A_{out} is extracted during the last iteration of the algorithm and squared to yield the intensity. A row from the two output intensities of the GS and the MRAF algorithms is depicted in figure 3.14 left and right, respectively. A row of the output was selected, which cuts through the rectangle horizontally. Comparison with the naked eye already reveals the higher smoothness of the output intensity of the MRAF algorithm. The smoothness of this **output** could be further increased by raising the number of iterations for the algorithms, however no observable difference in the **reconstructed** image quality appears in that case. To quantify the smoothness the root mean squared (rms) error (eq. 3.50) of the bright pixels, from their average value is calculated. For the output of the GS algorithm a rms error of 11.8% is obtained, while the MRAF algorithm reduces the rms error to 2.0%. However, in this example the GS algorithm performed 100 iterations of the Fourier transform loop, while the MRAF algorithm was deemed converged after 60 iterations. Comparing this increase in smoothness with figures 3.12 and 3.13, which show the reconstructed intensities of the GS and the MRAF algorithm respectively, shows that other factors limit the quality of the holograms, since the improvement there is much lower. Further improvements on the algorithms are necessary, as can clearly be seen from the above figures. Tricks on how to improve the MRAF algorithm are presented in section 5.4.
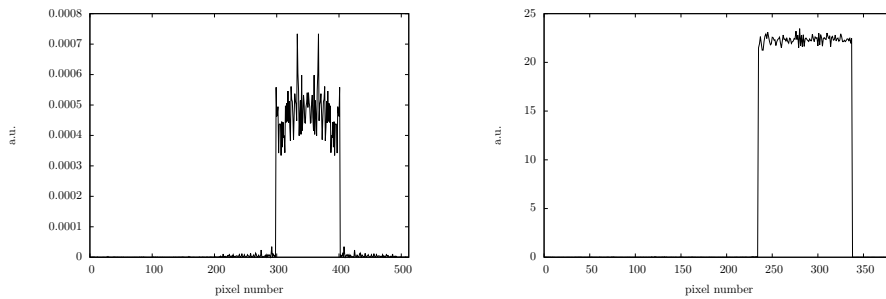
Figure 3.14: **Qualitative comparison of the smoothness of the presented algorithms** A cut through the output intensity of the GS (left) and MRAF (right) algorithms are plotted respectively. A horizontal line roughly through the center of the pattern, shown in figures 3.13 and 3.12 a) was selected. It is immediately visible, that the output of the MRAF algorithm contains much less relative roughness in the homogeneous areas of the rectangle. The GS algorithm underwent 100 iterations for this output, while the MRAF algorithm was terminated after 60 iterations.

Chapter 4

Liquid Crystals, Interaction, our Device

To introduce the liquid crystal spatial light modulator, which is the main subject of this thesis, an introduction to liquid crystals is given, their interaction with light is described and finally the device itself is introduced. Unless stated otherwise this section follows [22].

4.1 Introduction

In 1888 Friedrich Reinitzer found, that cholesteryl benzoate behaved rather strange when heated. Instead of simply changing from solid to liquid state at a certain temperature the substance would turn liquid and opaque at $145°C$ and turn clear at $179°C$. He reported his findings to Otto Lehmann, who studied the phenomenon and coined the term *liquid crystal* [17].
This name indicates the seemingly incompatible properties of these substances. On the one hand they are liquid, that means the molecules are not arranged in a rigid lattice but move freely among each other. On the other hand, liquid crystals show optical phenomena characteristic to crystals, such as birefringence. Devices based on liquid crystals have become basically omnipresent in our world, allowing for digital screens of unprecedented size. Neither the large screens of modern tv-sets nor the incredibly small screens of smartphones and wristwatches would be possible with cathode ray tubes.

4.2 Interaction with light

The characteristic property of liquid crystal materials is that almost all of them, especially all those which shall be considered here, are comprised of elongated molecules. In the treatment presented here they will therefore be approximated as stiff rods. While these molecules can have arbitrary relative positions, which

leads to the liquid characteristics, they prefer to orient themselves along each other, depending on the environmental situation, e.g temperature. (cf. figure 4.1) This gives rise to the crystal characteristics, as I will show below. Three
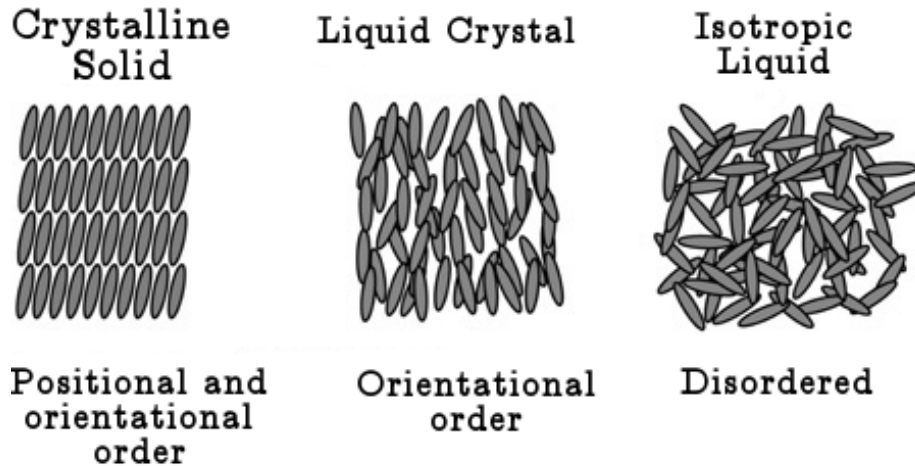

Figure 4.1: **Phases of a liquid crystal material.** At low temperatures the material behaves like a crystaline solid with positional and orientational order. At high temperatures the material behaves like an isotropic liquid, viz. no positional and orientational order at all. Unlike other substances however liquid crystals exhibit a mesophase, with no positional but orientational order. Adapted from [18]

main types of liquid crystal phases can be identified today: Nematic, smectic and cholesteric phases.

In a nematic phase the molecules exhibit no positional ordering. This situation is depicted in the center of figure 4.1. While the molecules orient themselves along each other their positions are arbitrary.

In smectic phases the molecules' positions are structured into layers along the molecules' long axes, that means, along the direction perpendicular to the layers the smectic phase exhibits a periodic structure. Within these layers the positions of the molecules are not fixed and no periodic structure forms.

In cholesteric phases no positional ordering appears and in contrast to the aforementioned phases the molecules do not try to align along each other but express a helical structure with a periodicity of a few hundred nanometers.

In the following I will focus on the nematic phase (cf. figure 4.1 center), because all relevant phenomena can be explained there and the liquid crystal used in the spatial light modulator, characterized in this thesis, is using a nematic-type liquid crystal.

The direction of orientation is called nematic director and is indicated in figure 4.2 through the arrow labeled **n**. It is possible to image **n** and such an image (Figure 4.3) reveals, that the director is not constant through a macroscopic
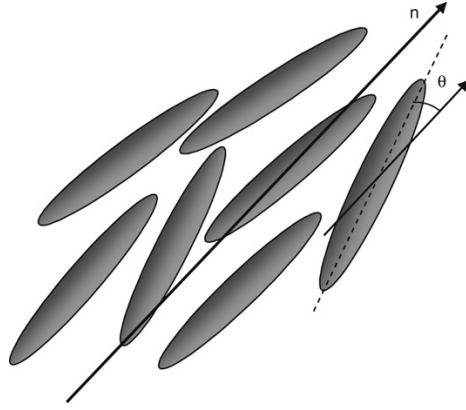
Figure 4.2: **Director of a liquid crystal** In a nematic phase liquid crystal a preferred direction of orientation of the molecules can be identified and it is denoted as a vector **n** called **director**. From the angle θ between the molecules and the director an order parameter can be derived. From [18]

sample, however it changes only slowly, compared to the size of the molecules.

Unsurprisingly this mutual orientation gives rise to optical phenomena like birefringence. It is therefore useful to quantify the degree of orientation. To do so a function $\omega(\theta, \varphi)$ in spherical coordinates is defined, where $\theta = 0$ corresponds to the direction parallel to the director **n**. (Figure 4.2)

$$\omega(\theta, \varphi) \sin \theta d\theta d\varphi \qquad (4.1)$$

Equation (4.1) describes the fraction of molecules whose axis lies within the interval $d\theta d\varphi$. Since the molecules are assumed to be uni-axially symmetric we define:

$$\omega(\theta, \varphi) = \frac{\omega'(\theta)}{2\pi} \qquad (4.2)$$

This distribution function can be expanded in Legendre polynomials

$$\omega'(\theta) = \sum_{l=0}^{\infty} \frac{1}{2}(2l+1) S_l P_l(\cos \theta) \qquad (4.3)$$

where the expansion coefficients S_l are given by

$$S_l = \int_{\theta=0}^{\pi} P_l(\cos \theta)\, \omega'(\theta) \sin \theta d\theta \qquad (4.4)$$

Independently of ω', $S_0 = 1$ always holds.
For nematic phases it also holds that $\omega'(\theta) = \omega'(\theta - \pi)$. From this follows, that S_1 vanishes. The first non-trivial contribution to this expansion is therefore:

$$S_2 = \langle \frac{3\cos^2 \theta - 1}{2} \rangle \qquad (4.5)$$

39

Figure 4.3: **Visualization of the director field of a liquid crystal.** There are various processes that allow the imaging of the director field of liquid crystals. The big black lines are results from polarizing optical microscopy and show the spatial variation of the polarization of the light propagating through the sample. In the technique applied for this image the fine lines are perpendicular to the director field and therefore allow its reconstruction. The inset in the upper right corner shows the director lines at the singularity or disclination. From [13]

S_2 will be our nematic ordering-parameter since it has the correct behavior in the limits of isotropic distribution, where it goes to zero and perfectly homogeneous distribution, where it goes to one.

After further steps of calculation, for which I refer the reader to the source of this section [22] it follows:

$$\Delta n = \Delta n_{max} \cdot S_2 = \left(n_{\parallel} - n_{\perp} \right) \cdot S_2 \tag{4.6}$$

The different refractive indices can be obtained from the Debye equation, which relates the microscopical polarizability α to the permittivity ε_r, which enters into the refractive index through $n = \sqrt{\varepsilon_r \mu_r}$.

$$\frac{\varepsilon_r - 1}{\varepsilon_r + 2} \frac{M_m}{\rho} = \frac{N_A}{3\varepsilon_0} \left(\alpha + \frac{\mu^2}{3kT} \right) \tag{4.7}$$

Here M_m and ρ are the molar mass and the density of the medium, N_A, ε_0, k and T are Avogadro's number, the vacuum permittivity, Boltzmann's con-

stant and the absolute temperature. μ is the permanent dipole moment of the individual molecules. α is the polarizability of the medium's molecules, which depends on factors like the difficulty to separate charges in a molecule through electric fields.

For LC materials μ and α are much greater along the molecules' long axis, compared to the directions perpendicular to it, which in turn means a higher refractive index along this axis. Together with the LC molecules' tendency to align along each other this gives rise to macroscopic birefringence.

The liquid properties of LCs however are essential to their usefulness in today's applications, such as liquid crystal displays (LCD). The fact that the LC molecules are not tightly bound to each other makes it possible to manipulate them rather easily. For an application such as a spatial light modulator, where a pattern of phase shifts or amplitude modulations is imprinted onto a wavefront, it is necessary to manipulate the liquid crystals with high spatial resolution, while assuring that this manipulation leads to the same results everywhere in a device.

To ensure uniform behavior of a spatial light modulator the orientation of the director, which is depicted in figure 4.3, needs to be the same over the size of the desired device. This can be achieved with very simple means. When a liquid crystal is placed onto a substrate its molecules tend to align along structures in the substrate. That means, by polishing or brushing the substrate along a direction, thereby creating microscopic ridges in the substrate, the LC molecules can be oriented along a single direction over macroscopic distances.

Control over a wavefront is exerted by varying the experienced index of refraction for light propagating through the LC material. An increased or decreased index of refraction yields a phase shift through the changed optical path length, which is $L_\nu = n_m \cdot L_m$ with L_m the physical path length, viz. the path of the light through the LC material and n_m is the index of refraction.

The index of refraction can be changed for the extraordinary axis, by rotating the liquid crystal molecules such that their long axis and with it the axis of high refractive index aligns with the direction of propagation of the light. This is depicted in figure 4.4. When a voltage is applied across the LC material its high polarizability will lead to a separation of charges and a following reorientation of the molecules along the electric field. Even if the voltage is applied along an axis perpendicular to the director a realignment will occur, since not all molecules are oriented perfectly along the director.

The top row of figure 4.4 illustrates this situation, where light propagates along the horizontal axis. The bottom row illustrates the respective indices of refraction, with the light propagating into the plane of the image. In the case of no voltage across the liquid crystal the molecules align along the vertical axis and pronounced birefringence occurs. The more the molecules align with the light's direction of propagation the smaller the birefringence gets, until it vanishes. While the ordinary index of refraction n_o remains unchanged the extraordinary index n_e decreases.

If one illuminates the liquid crystal with light polarized along the extraordinary axis only, this method allows phase retardation and with spatially resolved con-
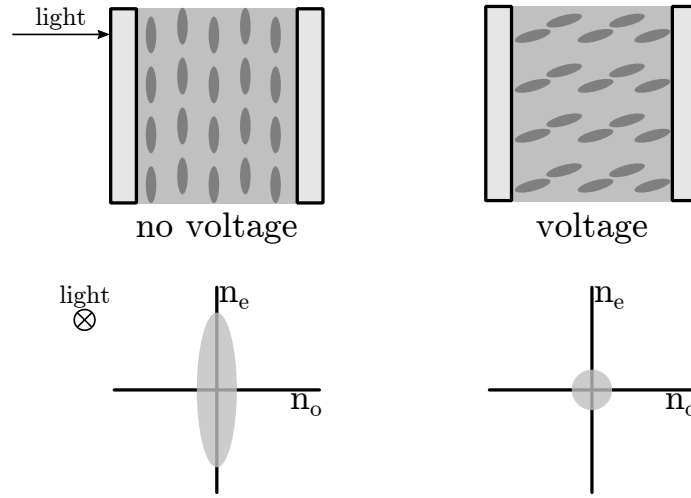
Figure 4.4: **Schematic view of a SLM pixel** In the upper half the effect of applying a voltage across a pixel is depicted. The voltage will induce temporary diplolar moments and the molecules will rotate to align with the electric field. In this case the light propagates along the horizontal direction through the pixel. In the lower half the respective refractive indices are shown. Here the ordinary and extraordinary axis correspond to the pixel, shown above, rotated by 90° around the vertical axis. Accordingly the light would be propagating into or out of the page plane. With the projected length of the molecule decreasing with rising voltage the birefringence will vanish. Or, if only light polarized along the extraordinary axis is considered, the refractive index and with it the effective phase shift of the light decreases. (adapted from [16])

trol over n_e the imprinting of a phase pattern. The amplitude of a light field can be modulated with the same device. By illuminating it with circular polarized light a relative phase between the ordinary and extraordinary components of that light can be introduced, changing the orientation of polarization. Together with a quarter-wave plate and a polarizing beam splitter spatially resolved amplitude modulation can be implemented. This was used in section 5.2 and the mentioned setup is depicted there, in figure 5.6. Thanks to microfabrication techniques electrodes on the order of micrometers can be created, which means that the index of refraction for extraordinary polarized light can be controlled with pixels on these length scales and the aforementioned techniques can be implemented. With this the encoding problem of chapter 3.6 is addressed.

4.3   The spatial light modulator

In the preceding sections a theoretical framework was established, that allows the description of devices that can be electronically controlled to create light

fields of arbitrary geometry through holographic methods, called *spatial light modulators* or SLMs.

4.3.1 Hardware

The device, this thesis is centered on is the XY series 512×512 spatial light modulator, manufactured by *Boulder Nonlinear Systems*. It is depicted in figure 4.5. It features an active area of 7.68×7.68 mm^2 comprised of 512 by 512

Figure 4.5: **The** 512×512 **XY-series SLM by Boulder Nonlinear Systems** It features 512 by 512 pixels based on LCoS (Liquid Crystal on Semiconductor) pixels that can be addressed with 65536 levels. The small reflective area at the very front of the device is the active region, which houses the liquid crystal pixels.

reflective pixels, which can be seen in the image as the reflecting square at the very front of the device. It follows that each of these pixels is $15\mu m \times 15\mu m$ in size. The active area is mounted on a tilt stage, which allows the rotation of the active area around the two axes of the reflective surface which can be controlled via two precision screws, labeled "V" and "H" for the vertical and horizontal

rotation.

Electronic addressing of the pixels is done via two stages of electronics. Directly behind the tilt stage is a circuit board, that relays the signals from the driver box to the active surface via a flat ribbon cable.

A second flat ribbon cable connects the relay electronics to the driver box, which also provides power for the SLM. The driver board receives signals from a computer via USB or DVI connections. In our device the connection to the computer is implemented via DVI, which means, that the computer actually detects the SLM as an external monitor. It was actually possible to move the mouse cursor to the active surface of the SLM and the moving cursor could barely be observed with the naked eye with room light.

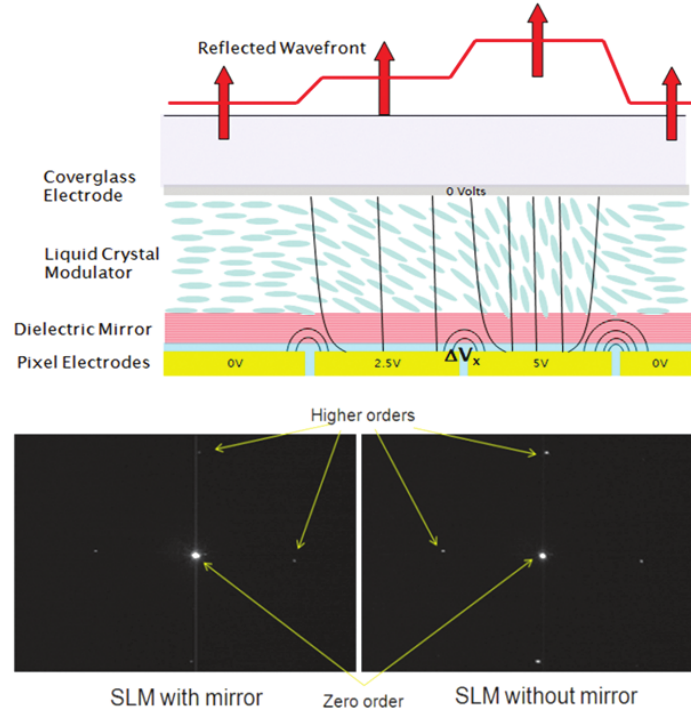Since the back panel of the active surface is comprised of pixelated electrodes,

Figure 4.6: **Cross section of the SLM's active surface** In order to reduce diffraction from the pixel structure (reflective pixels) an additional homogeneous mirror coating is applied to the back wall of the liquid crystal cell. In the bottom row the lower intensity of light diffracted from the pixel structure can be seen. From [15]

to ensure spatially resolved control over the liquid crystal's orientation, large diffraction from this grating structure is to be expected. In order to reduce this effect a mirror coating is applied on top of the pixel structure, which does not interfere with the electric fields, controlling the liquid crystal but screens

the electrodes themselves from the light, illuminating the SLM. (cf. figure 4.6) According to the manufacturer the amount of light scattered from the electrodes is reduced from 39% to 10%.

4.3.2   Software

The SLM is controlled via software, called *BLINK*, that was provided by the manufacturer. The software provides a straightforward interface to load and display phase patterns on the SLM. In BLINK the control over the phase shift of the SLM is exerted via bitmap files. Bitmap files are image files, which store 24 bits of color information per pixel without any compression. Each pixel has three 8 bit color values, for red, green and blue color, which comprise the image. The pixel wise voltage of the SLM can be controlled with 16 bit values (65536 steps) and these 16 bits are stored in two of the color values of the bitmap file:

$$\underbrace{11010001}_{green}\underbrace{10010111}_{red} = \left(\frac{53655}{65536}\right) \cdot 2\pi$$

The 8 higher valued bits are stored in the green channel of the image, while the 8 lower valued bits are stored in the red channel. Any information that is contained in the blue channel of the bitmap image is ignored by the software. This means, that a phase pattern will appear in tones of red, yellow and green in the preview, as can be seen in figure 4.7. This figure also shows the graphical user interface of BLINK. Moving counter clockwise, from the top left, the provided features are:

- Specification of a directory, which contains the desired phase patterns

- Display of all detected image files in the directory chosen above

- A preview of the currently selected phase pattern

- Controls to display the patterns from the current directory as a sequence, with specified frame rate and number of loops

- Specification of a lookup-table to translate the desired phase shift into control voltages for the SLM

The lookup table is a tool to calibrate the SLM purely software-wise. An actual SLM will provide phase shifts of more than 2π in the range of its 65536 possible control voltages, which means, that a range of 2π phase shift needs to be identified and the phase pattern from the image file needs to be translated accordingly.
The manufacturer provides a simple lookup table with each SLM, which allows for quick setup and usage of the device. However, this lookup table sets the 2π range equally for all pixels and does not take into account the response of the individual pixels. In section 5.1 an advanced calibration scheme is presented, which allows, in principle, for the selection of an appropriate range of phase
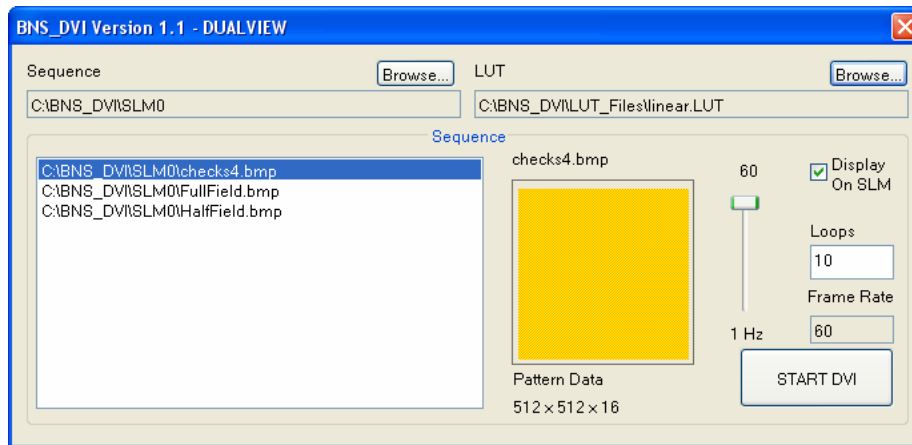
Figure 4.7: **BLINK GUI** The graphical user interface of BLINK allows for straight forward loading of phase patterns, via browsing the path of the phase patterns. The window on the bottom left shows all image files found in the specified directory. A preview of the selected phase pattern is given and controls are provided to display all image files from a directory as a sequence, with given frame rate and number of loops. BLINK also allows the specification of a lookup-table that translates the desired phase shift into the actual applied control voltage on the device.

shift for every individual pixel. It should be noted, that the response of the individual pixels does not vary wildly, as can be seen in figure 5.3. The ranges, where the phase shift rises approximately linearly, overlap in large parts, hence the manufacturer's lookup table is not, as it may appear after this discussion, useless.

Alternative beam shaping approaches

Before the experimental discussion of the SLM, alternative approaches to beam shaping shall be shortly discussed and the reason for selecting this device will be given.

The problem of beam shaping is fairly general and accordingly the tools for shaping beams are diverse. The first idea one might have, when thinking about shaping a beam is that of an aperture. Simply by attenuating parts of the beam such that a desired shape results is a straightforward approach, which is also supported by geometrical optics. Yet this idea reaches its limits with the limits of geometrical optics. For example, placing a rectangular slit into a beam path one will only create a rectangular beam very close to the slit itself. At some distance behind the aperture the effects of diffraction will start to appear and the typical diffraction fringes will distort the shape of the beam.

So while this seems a straightforward implementation of beam shaping, it also seems to be of very little practical use. Nevertheless it is widely used in lithographic microfabrication, where masks of desired shapes are applied directly on top of a substrate material, to create microscopic structures, for example in microchips.

Another approach, which is usually not discussed as beam shaping, are lenses. Simply focusing a beam to create a small spot at a desired location is de facto shaping a beam, although it is not a very flexible approach, since only one kind of shape can be produced and only at one location.

An extension of this notion are cylindrical lenses. Instead of focusing a beam in both transversal directions as spherical lenses do, cylindrical lenses focus a beam only along one axis. If one were to place two cylindrical lenses, focusing along orthogonal axes in a beam path, such that their focal points do not coincide, elliptical beams can be created. This situation is shown in figure 4.8. In the region between the two focal planes three characteristic points will occur: At the first focal plane the light will be at its tightest focus along the first axis, while still being partially expanded along the second, yielding an elliptical spot along the second axis. At the second focal plane the exact opposite happens and while the light is tightly focused along the second axis the beam has already expanded along the first, yielding another elliptical spot, now along the first axis. Between these two points there will be a plane, where the beam is partially focused along both axes, such that a radially symmetric spot appears.

This approach is currently in use in our experimental setup, to illuminate a
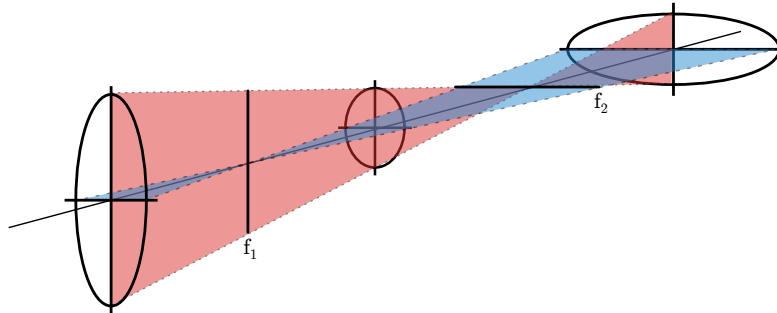

Figure 4.8: **Elliptical foci from cylindrical lenses** When two cylindrical lenses are placed such that the focus the light along orthogonal axes and their focal planes do not coincide two elliptical foci appear, where the light is focused along one axis, while being partially defocused along the other. Between those two points a radially symmetric focus will appear.

string of ions, with high light efficiency. But, starting from a gaussian beam, the elliptical spot will still exhibit a Gaussian profile in its cross sections.

To further improve on this so called diffractive elements can be employed. A simple example for a diffractive element would be a diffraction grating, but more complex elements are possible. Here holographic techniques can be em-

ployed, similar to the ideas described in chapter 3, to create transparencies, which imprint phase or amplitude patterns on an incident beam. The Fourier transforming ability of a lens will then create a desired pattern in its focal plane and the only limit to the created shape is the resolution of the optical system. Note that while I am talking about transparencies here, reflective elements are possible and differ only in that the outgoing light is reflected, instead of transmitted.

Fixed diffractive elements however require very precise alignment to work properly and are then only capable of producing one pattern.

The next improvement are the SLMs, one of which is the center of this thesis. They work fundamentally similar to diffractive elements but with the great advantage of being optically or electronically addressible. So while a diffractive transparency needs to be physically replaced if another beam shape is needed a SLM is simply reprogrammed.

While optically addressed SLMs, that means, devices, where the phase shift or transmission is set by controlling light, instead of an electric field, are not very useful for creating complex patterns (the addressing beam would need to be in the shape of the transparency's pattern, which is just as hard to realize as the original beam shaping problem) they serve for example as light valves, where a pulse of light changes the overall transmission of the SLM to control another beam [25].

Electronically addressed SLMs on the other hand contain microfabricated electrode structures, which allow a very high degree of control over the features of the created transparency. This means, that without physically touching the device a transparency can be created, integrated with the setup and altered. This allows complex procedures such as in situ aberration correction, as is shown in section 5.3.

Two major types of SLMs can be identified: Liquid crystal devices, such as the one introduced in the preceding sections, and digital micromirror devices. Digital micromirror devices are made up of arrays of micro-mechanical mirrors, which can be switched between two states, that means positions, electronically. Light is reflected in one of two directions and binary transmittivity structures can be created. Intermediate states can be interpolated by switching between the two states rapidly and setting the amount of time spent in each of the states accordingly. There are techniques to imprint phase shifts on a light field, such as the detour phase technique [20], where groups of pixels are combined into superpixels. Figure 4.9 clarifies this notion. The digital micromirror device's surface is divided into superpixels, which are made up of several actual pixels. Within one of these pixels three parameters control the amplitude and the phase of the light. The parameters p and q define a rectangle, from which light is reflected in the superpixel. The amplitude of the reflected light is directly proportional to the area of the rectangle $a = p \cdot q$. By displacing the rectangle from the center of the superpixel the phase of the light can be shifted. The displacement results in an effective detour of the light, which is equivalent to a shifted phase.

But this increased control comes at the prize of a greatly reduced pixel number
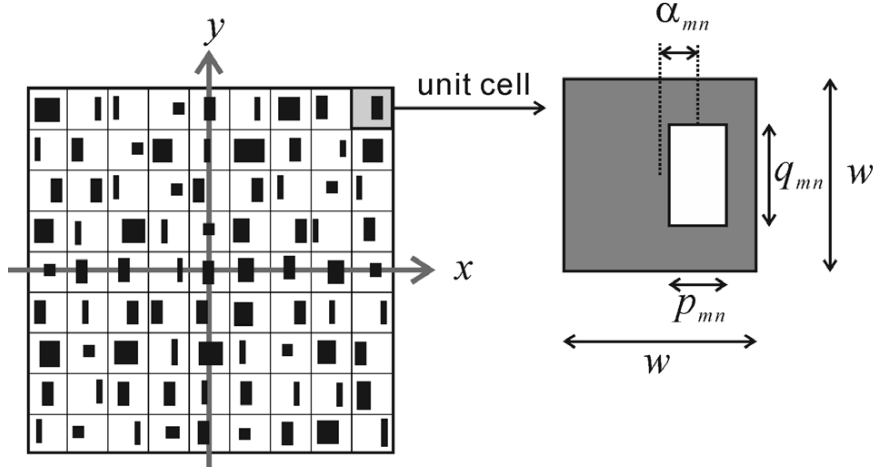
Figure 4.9: **Detour phase technique to imprint phases with DMDs**
Groups of pixels are combined to superpixels, denoted as "unit cell". Within
this superpixel the three parameters p,q and α control the amplitude and the
phase of the light, reflected from it. While p and q determine the reflecting area
and thereby the amplitude of the reflected light, α controls the phase. From [20]

and in effect increased sample distance. So for these techniques there is always
a trade-off between control over individual pixels and the number of usable pix-
els. For example creating superpixels from 4×4 micromirrors would reduce the
effective pixel count by a factor of 16. For a DMD-SLM of 2048×2048 pixels
this would result in an effective pixel number of 512×512, which is what the
device in this thesis offers, but with only 4 steps of phase control, instead of
65536.

In the case of liquid crystal SLMs typically only the phase of the light is con-
trolled, although amplitude control is possible. However, a strong reason for
phase instead of amplitude control is the fact that amplitude modulation dis-
cards parts of the incident light.

This is one of the reasons, together with the high flexibility and the possibil-
ity of aberration correction, why the device for this thesis was chosen over the
available alternatives and is to be assessed for its suitability.

Chapter 5

Experimental Results

5.1 Calibration and Lookup table

5.1.1 Calibration scheme

The first step in characterizing the SLM, that was introduced in the preceding section, is a calibration.

As mentioned before the SLM needs to be calibrated for two reasons. First, the liquid crystal pixels are able of performing higher phase shifts than 2π over the range of possible addressing values. Second the pixels may not correspond uniformly to applied voltages, which means, that a range of values needs to be identified for each pixel, which provides a phase hift of 2π and a table to translate the desired phase shift into the correct voltage needs to be created and implemented. A translation table, or *lookup table* (LUT), specially tailored for each device is provided by the manufacturer, but this LUT does not account for the inhomogeneities of the pixels' response to the control voltages. This is the second reason for the need of a calibration technique.

For this thesis a technique, developed by Gregor Thalhammer was implemented [23] [24].

The technique relies upon interferometry, to detect the the phase shift, induced by the SLM, relative to a reference picture. The setup is schematically shown in figure 5.1. Light from a polarization maintaining fiber is adjusted such that its polarization coincides with the vertical axis of the SLM, since this is the polarization of light, which is modified by the SLM. The beam is expanded and recollimated, using a simple telescope made from two positive lenses, to illuminate the entire SLM area homogeneously. The illumination need not be perfectly homogeneous for this technique, but it simplifies the detection at the CCD camera. The beam is split on a non polarizing beam splitter cube and the SLM's active surface, as well as a flat mirror are illuminated. The light reflected off both surfaces is recombined at the beam splitter and the interference pattern is imaged onto a CCD camera.

To resolve the spatial differences in phase shifts the lens of the camera is set
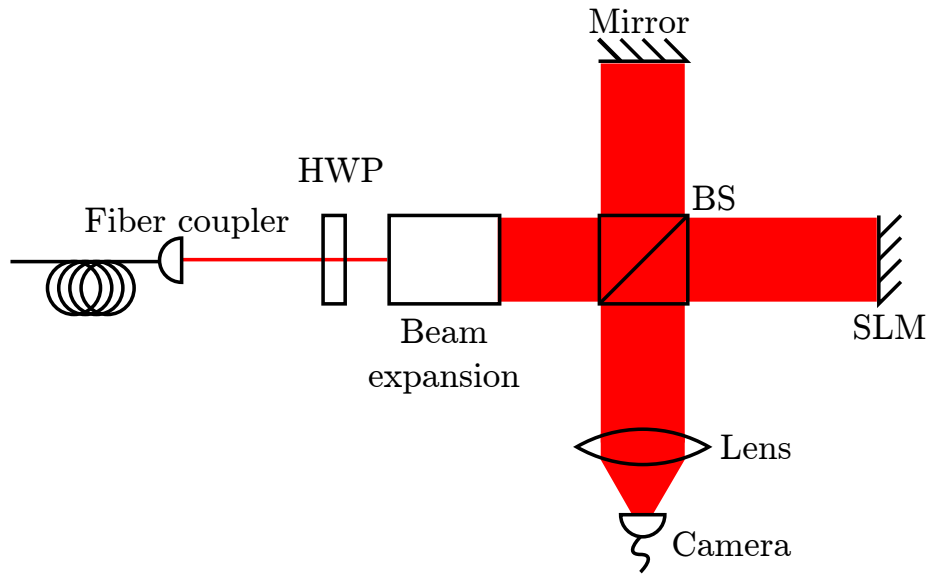
Figure 5.1: **Experimental setup to calibrate the SLM's phase shift** To spatially resolve the SLM's phase shifts it is placed in a Twyman-Green interferometer. An expanded collimated beam of laser light is split on a non polarizing beam splitter and illuminates the SLM, as well as a simple mirror. The reflected light is recombined at the beam splitter and the resulting interferometric pattern is imaged onto a CCD camera.

such that it images the SLM's surface onto the camera. Here a 50mm lens by Nikon was used, that was attached to the camera, via an adapter, from Nikon's f-mount, to the camera's c-mount.

Next a series of images is taken, each with another control voltage applied. Instead of recording the entire 65536 possible control voltages, 128 images were taken, by increasing the value of the highest valued bits of the 16 bit control values. Thinking of the bitmaps, mentioned in chapter 4.3 that means, that for each subsequent image the color value of the green channel was increased by 2, while the value of the red channel was kept at 0. This also implies, that the index of the image multiplied by two yields the corresponding value of the green channel. Figure 5.2 shows an example image for this calibration scheme. Sub-image a) shows the actual recorded image and many imperfections, such as diffraction from dust particles and a pattern from the background of the SLM are visible. To cancel the effect of these incoherent distortions to the interference pattern two reference pictures are taken. Sub-image b) shows the pure reflection from the mirror, while c) shows the reflection from the SLM. Some of the features of a) can be identified immediately and d) shows the interference pattern after subtracting b) and c) and some cropping. It is immediately visible, that the clarity of the interference pattern is increased greatly. Since the
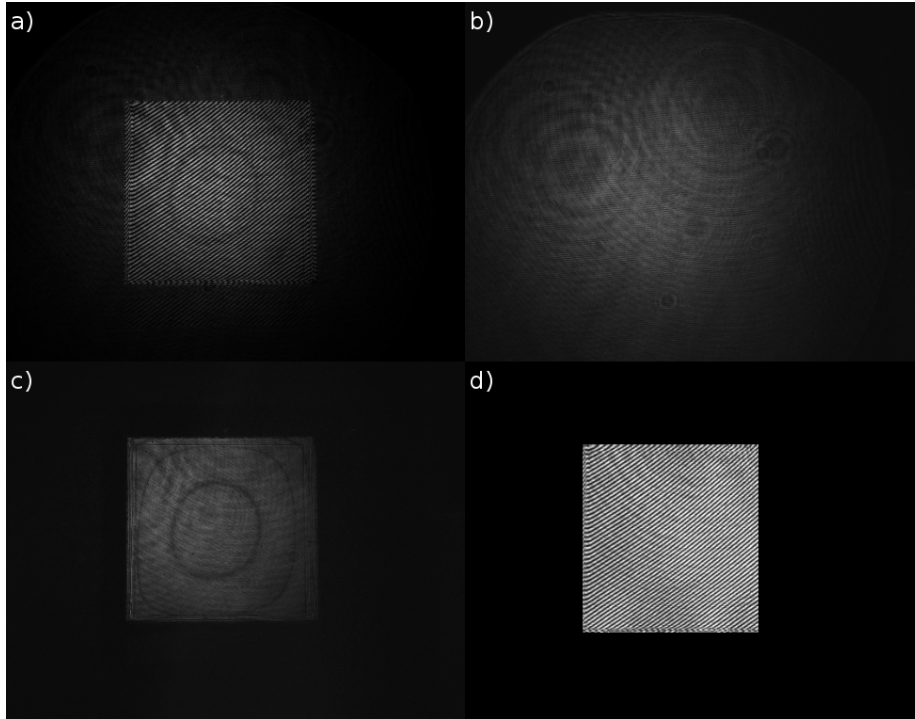
Figure 5.2: **Sample images for the calibration scheme** Sub-figure a) shows a recorded image for the SLM calibration. Several features can be identified, that do not stem from interference of the two beams. To cancel these incoherent distortions images b) and c) are recorded, which show only the light from the mirror and the SLM respectively. In d) the remaining interference pattern is shown and the improvement is clearly visible.

relative alignment of the SLM and the mirror will never be perfect, especially not by interferometric standards, a relative tilt between the two is deliberately induced. This allows for a simple reconstruction of the relative alignment from the direction of the interference fringes and through that a subtraction of this background from the interferometric images.

Due to limited resolution of the camera available only sets of 16×16 pixels could be recorded. Figure 5.3 shows the reconstructed curves of phase shift, plotted against the index of recorded images. The 127 data points are interpolated by third order splines to allow the determination of addressing values for any desired phase shift. A rather large variation in the response of the pixels can be observed here, with the maximum phase shift differing by about π. The small bumps that appear in all curves for certain values are remnants of disturbances during the recording process. Since they appear at the same time for all pixels no relative phase shifts will be introduced by them and no distortion of images
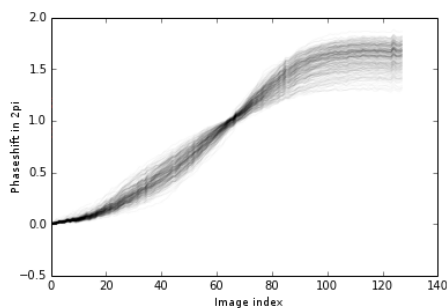
Figure 5.3: **Subset of the recorded curves of phase shift** This figure shows the recorded phase shift, in units of 2π, plotted against the index of the recorded image. A large section of near linear rise of the phase shift with addressing index can be seen, which is beneficial for the construction of a lookup table. It can also be seen, that the variation in behavior of the pixels is rather pronounced, with a variation in maximum phase shift of about π. A value close to the beginning was chosen as the onset of the 2π range for all pixels, to make sure that all pixels start at the same phase shift.

is to be expected.

5.1.2 lookup table

From the recorded data a table needs to be constructed, which allows the translation of the phase shifts, created by the iterative algorithms introduced in chapter 3.7 into addressing values for the SLM. Due to the limited resolution of the calibration data as well as the limited usable range of the addressing values the output of the algorithms is limited to 8 bit values, that means 256 steps between 0 an 2π. This still allows an approximation of the exact value to less than 0.03 radians.

To simplify the translation a range of values is selected, where the phase shift rises approximately linearly by 2π, which is easily identified from figure 5.3. Each curve is inverted and the 2π range is split into 256 values. The corresponding addressing values are then stored in the LUT file. The onset of all curves was chosen to be the same for all pixels and a value was chosen, where the individual phase shifts had not diverged too far. Any remaining offsets between the pixels would manifest as optical aberrations and can be corrected for with the scheme, presented in section 5.3.

The resulting file consists of 32×32 arrays of numbers, which associate 256 steps of phases with the according addressing values. It is now straight forward to interpret the number from the LUT file and create a bitmap file, which contains the correct addressing values in its green and red color channels. Figure 5.4 shows a bitmap file, after translation through the LUT, created from this scheme. The input file was set to create a uniform phase shift of π for all pixels. The reduced size of 32×32 allocation units is readily identified through the
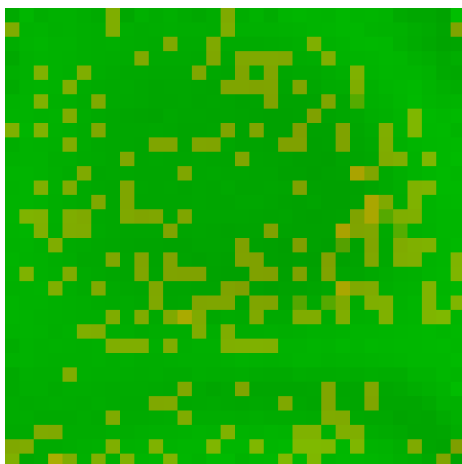
Figure 5.4: **Example file for LUT translation** The original file contained a gray value of 127 for all pixels, corresponding to a homogeneous phase shift of π for all pixels. After translation through the LUT the features of the calibration become visible. The finite size of the LUT, assigning one value to 16×16 pixels manifests in the boxes of constant color. The large structures of darker green values as well as the different shades of orange hint at the nonuniform response of the SLM

square structure. In the bottom of the image, as well as the top right corner large structures of darker green values can be identified. These structures stem from the non-uniformity of the 2π range, which was the reason for the creation of the LUT.

5.1.3 Comparison to lookup table from BNS

To conclude this section the LUT created by this technique will be compared to the LUT, which was provided by the manufacturer. As a figure of merit the efficiency of a one dimensional blazed grating was chosen.

A series of images was taken, imaging the light reflected off the SLM and diffracted from the displayed grating. As a reference picture the pure reflection was recorded, seen in figure 5.5 a). Sub-figures b) and c) show the light diffracted from a blazed grating for the manufacturer's calibration and the manually calibrated SLM respectively. The brightness and contrast of these images were enhanced for visual comparability. For quantitative comparison however it was ensured, that no pixels in the images were saturated and the respective times of exposure and gain levels were recorded and taken into account. As a measure of diffracted power the overall intensities of the spots were calculated, by summing up all pixels in an area around these spots. A background image, without any light from the SLM was taken and subtracted from all images.
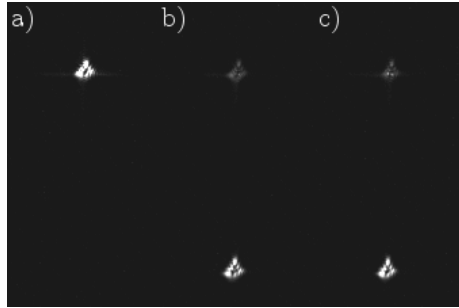
Figure 5.5: **Sample images for the comparison of diffraction efficiencies**
Sub-figure a) shows the reflected spot, when no pattern is displayed on the
SLM. Sub-figures b) and c) show the undiffracted light at the top of the image
and the first diffraction order from a one dimensional blazed grating, from the
manufacturer's lookup table and the calibration done here, respectively, at the
bottom.

The respective diffraction efficiencies were 67.1% for the manual calibration and
69.2% for the manufacturer LUT. Within the observed fluctuations of the in-
cident laser intensity these values are indistinguishable. This means, that at
this point the calibration scheme of Gregor Thalhammer did not provide an ob-
servable advantage. However, a more detailed calibration, that combines fewer
pixels could improve that situation.
Note also, that these numbers are not significant as absolute diffraction effi-
ciencies, since the blaze angles were not optimized. However, since both used
gratings used the same blaze angle the values are meaningful in terms of com-
parison among each other.

5.2 Phasejitter and modification

In the interaction between ions and lasers (cf. section 2.3) two kinds of rotations
on the Bloch sphere are possible, corresponding to the angles, that characterize
the superposition state. Rotations about the z-axis, changing the angle ϕ are
realized through light shifts. To rotate the state around the x- and y-axes the
coherent excitation of the $S_{1/2}$-$D_{5/2}$ transition is used. However, to fix the axis
of rotation precise control and knowledge over the laser and ion's phase evolu-
tion are necessary and great efforts are taken to ensure their stability.
Since the SLM heavily modifies the phase of the interacting light field the re-
sulting phase stability needs to be assessed.
The absolute value of the relative phase is not an issue here, since this value
simply defines the initial value of ϕ relative to which rotations are taken during
an experiment. The only concern here is dynamical changing of the phase due
to effects in the SLM.
The reason for this concern is a property of liquid crystal pixels, that was not

addressed before. When an electric field is applied across a LC pixel, the LC molecules will align along the field, as was mentioned before. However, between the electrodes and the LC molecules in direct proximity to them chemical reactions can occur, which would in rather short time destroy the electrodes, as well as the LC material.

To overcome this problem LC pixels are driven by AC voltages, instead of DC. One would expect an AC voltage to simply cause the LC molecules to jitter around their initial orientation, but the process of separating the charges on the LC molecule occurs in much shorter time, than the actual rotation of the molecules. So in the moment, the polarity of the electric field changes the charges on the molecule will switch places much faster than the molecule can rotate due to the changed force, yielding a net orientation of the molecules.

There is of course some remaining jitter of the molecules, due to the varying electrostatic force, which occurs in all liquid crystal devices, such as computer monitors. In consumer products however this effect is negligible, since the human eye is far to slow to resolve the transmission changes, accompanying this jitter.

For the scientific grade devices of boulder nonlinear systems and other manufacturers special measures are taken to minimize this phase jitter. The SLM that was introduced above operates its drive AC voltage at a frequency of 6 kHz, compared to about 100 Hz for LCDs in notebooks and smartphones.

To gain maximum sensitivity to instabilities in the phase of the reflected light
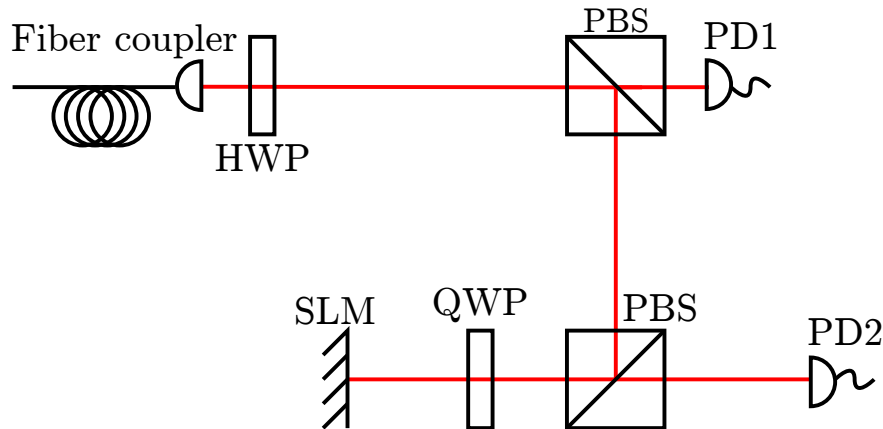

Figure 5.6: **Setup to determine the stability of the SLMs phase shift** A quarter wave plate is used to illuminate the SLM with circularly polarized light. Only the vertically polarized part of the light will experience a phase shift and therefore the net polarization will change, depending on the induced shift by the SLM. On its second pass through the QWP the light is turned to linear polarization again. A polarizing beam splitter (PBS) separates the horizontal and vertical parts and the reflected light is detected on the photodiode PD2. The photodiode PD1 is used to filter intensity fluctuations of the incoming laser.

the setup of figure 5.6 was used. Instead of illuminating the SLM with linearly polarized light a quarter wave plate (QWP) was placed directly in front of the active surface. Incoming linearly polarized light is converted to circular polarization and hits the device. Since only the vertically polarized part of the light will encounter phase retardation the net polarization changes. After a second pass through the quarter wave plate the light is turned into linearly polarized light of another orientation, depending on the experienced phase shift. The polarizing beam splitter cube (PBS) separates horizontal and vertical polarziation and a photodiode (PD2) detects the reflected intensity. The photodiode PD1 was used to filter out intensity fluctuations due to fluctuating transmission through the polarization maintaining fiber, providing the light. Figure 5.7 shows a section of the time resolved phase shift of the SLM. A modulation with a frequency of 1015 Hz is clearly visible. The dependence of the modulation on the induced phase shift was measured, to back up the notion that it originates from the SLM. The
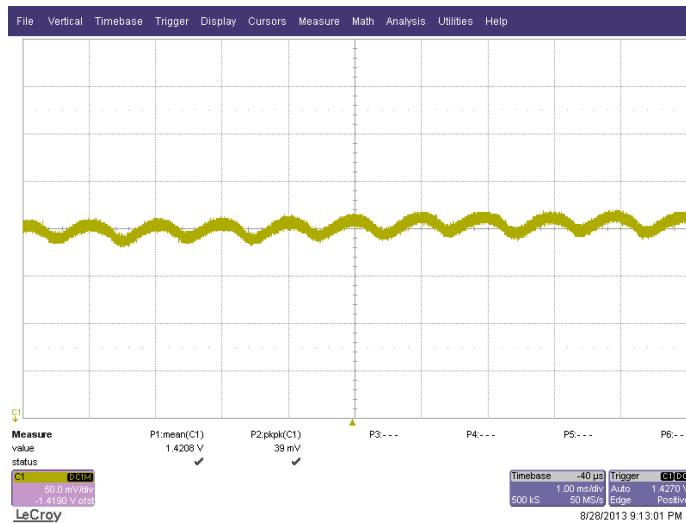

Figure 5.7: **Time-resolved trace of the SLM's phase shift** Unfortunately a modulation of the phase shift at 1015 Hz is visible. Its origin was found to be an image refreshing rate, which was set by the manufacturer. This trace was taken with 1 Millisecond time, per horizontal section and 50 Millivolts per vertical section.

behavior of the modulation fulfills the expectations. With rising phase shift the modulation decreases, since a higher phase shift corresponds to a lower applied voltage. The maxima of the modulation coincide with the regions where the transmission changes the most with the phase shift, while the minima coincide with the extrema of the transmission curve.

After consulting the manufacturer the source for this modulation could be identified. The voltage, applied to the SLM actually changes with three distinct rates, which are:

- The basic drive voltage, in this case 6kHz, which ensures the integrity of the liquid crystals and is set to minimize jitter

- A manufacturer-set image refresh rate, at which the currently displayed image is reloaded

- The software-set frame rate, which ranges from 0 to 30 Hz for this model

The image refresh rate renews the currently displayed image at a rate which is an integer multiple of the basic drive rate. In order to do that the displayed image is completely erased from the SLM and reloaded. This rate was initially set to exactly 1015 Hz and was identified as the source of the observed phase jitter. To reduce its effect on the phase stability the device was sent to the manufacturer and the image refresh rate was reset, to reduce the remaining phase jitter. Since the refresh rate needs to be an integer divisor of the drive rate it was changed to 1.5 kHz, taking into account minimal residual jitter as a guideline.

To quantify the jitter and its reduction by the manufacturer the transmission curve was linearized around the point of steepest change and the modulated transmission signal was translated into a modulated phase shift. For the SLM before the modification the phase jitter was measured to be 0.159 rad or 9.1°. After the modification the jitter was found to be 0.123 rad or 7.1°.

If this phase shift proves to be detrimental to qubit operations further modification must be considered.

5.3   Aberration correction

Aberrations are a serious limitation to the performance of optical systems, as mentioned in chapter 3.5. These deviations of an optical system's behavior from the ideal model of spherical lenses leads to major distortions of focal points and plane waves.

Usually aberrations are quantified by determining the Zernike coefficients of a wavefront. This allows for an easy comparison between different systems or states before and after correction. However, for this approach it is usually necessary to place a sensor, capable of detecting a wavefront, at the location of interest. This poses a problem in setups where access to a point of interest is restricted, as is the case in our experiment. Placing a wavefront sensor at the location of the ions is impossible due to the trap itself, which only leaves a few cubic millimeters of space around the ions, as well as the vacuum vessel, which can not be opened ad libitum. Still, correcting aberrations is very much desired in our experiment, since badly shaped elliptical beams reduce light efficiency and can lead to stray light from reflections, which reduces our experimental control.

Fortunately there is a way to measure and correct optical aberrations with the SLM, which can be applied in our setup. This technique relies on a single point-like detector to measure the distortion of a wavefront. This means, that by

employing a single trapped ion as the detector it becomes possible to measure the aberrations in the complete beam path, from a fiber to the ions, including the vacuum viewport, without opening the vacuum vessel.

5.3.1 Measuring with a single ion

The description of this technique follows the master's thesis of Philip Zupancic [27]. While in his thesis the technique was applied to a DMD SLM and neutral atoms in a magneto-optical trap its principles are readily transferred to a liquid crystal SLM and trapped Calcium ions.

The fundamental principle behind this technique is to divide the active surface of the SLM into a number of patches and determine their relative phase shifts. In the limit of infinitesimal patches the wavefront would be reconstructed perfectly, however in practice this is neither possible nor necessary. The setup used to implement this scheme in a test setup is shown in figure 5.8. The SLM is
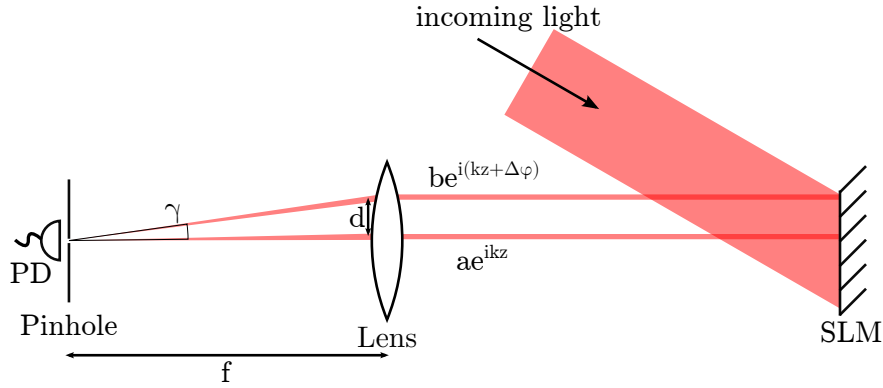

Figure 5.8: **Setup to test the scheme for aberration correction, adapted from [27]** To separate the light of the patch to be measured and the reference patch from the remaining reflected light a diffraction grating is displayed on the patches and the first diffraction order is imaged onto a Photodiode with a pinhole, which simulates the point-like detection, realizable with a single ion. Additionally a beam profiler is used to view the generated spots. Examples of the created spots, as well as the phase pattern used for this technique are depicted in figure 5.9. The undiffracted light is not depicted for clarity.

illuminated with light, polarized along the liquid crystals' extraordinary axis (vertical) and a diffraction grating is displayed on the reference patch, as well as the currently measured patch. The diffracted light is imaged onto a photodiode (PD) with a $5\mu m$ pinhole, which simulates the pointlike detector, a single ion would be. Figure 5.9 shows sample images to clarify this approach. In sub-figure a) the phase pattern is depicted. Only light that illuminates the two grating patches gets diffracted and gets imaged onto the pinhole. The patch

in the center of the pattern is used as a reference, to which all other patches are compared. If only one of those patches is present on the pattern, a spot like in sub-figure b) forms in the focal plane. This spot is rather large, since its size is limited by the small dimensions of the diffracting patch. In this case the patch has a size of 32×32 pixels on the SLM, which corresponds to $480\mu m$ edge length on the SLM. If both patches are present their focus spots will overlap and produce interference fringes, as seen in sub-figure c). The pinhole in front of the photodiode corresponds roughly to one pixel in this image. If the detector is small enough, meaning shorter than half the wavelength of the shortest interference fringes produced, the sinusoidal shape of the fringes can be reconstructed, by shifting the phase of the light from the two patches. The
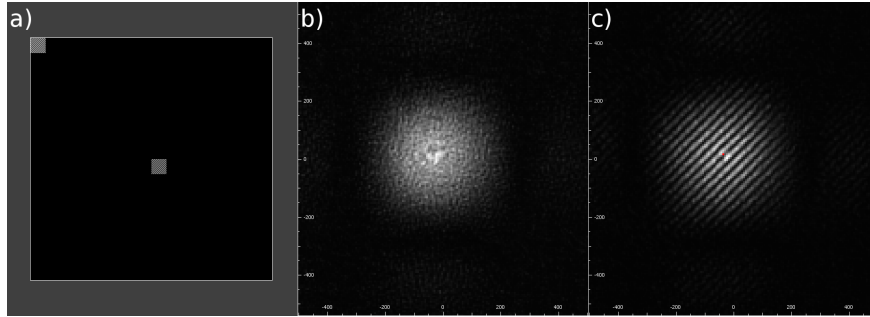

Figure 5.9: **Example images for the aberration correction scheme** Sub-figure a) shows the phase pattern, used to measure the relative phase shifts of the designated patches on the SLM surface. The center patch is used as a reference for all measurements, while the patch on the top left is the currently measured patch. Each of these patches produces a spot in the focal plane of the lens, which is seen in sub-figure b). When two of these spots overlap they produce interference fringes, which can be sampled with a small detector. The detector in the test setup corresponds roughly to one pixel in sub-figure c).

fringes follow from the equation

$$I\left(x, z\right) = a^2 + b^2 + 2ab \cos\left(\frac{2\pi}{\lambda}\left(z\left(1 - \cos\gamma\right) + x\sin\gamma\right) + \Delta\varphi\right) \qquad (5.1)$$

where z is the direction of propagation of the light after the SLM and x is the distance of the measurement patch from the reference patch on the SLM surface. ae^{ikz} and $be^{i(kz+\Delta\varphi)}$ are the fields of the reference and measured beam respectively, as seen in figure 5.8. The angle γ is defined as the relative angle under which the light from the two patches is incident onto the photodiode. Obviously a single measurement is not sufficient to reconstruct the phase of the fringes. However, sampling the interference fringes at three points, yielding three intensities

$$m_1 = a^2 + b^2 + 2ab\cos(\Delta\varphi)$$
$$m_2 = a^2 + b^2 + 2ab\cos(\Delta\varphi + 2\pi/3)$$
$$m_3 = a^2 + b^2 + 2ab\cos(\Delta\varphi + 4\pi/3)$$

allows the construction of a phasor p, which contains the amplitude and phase of the fringes:

$$p = -\frac{1}{3}(m_2 + m_3 - 2m_1) + \frac{i}{\sqrt{3}}(m_2 - m_3) \tag{5.2}$$

The phase can be extracted from this, via $\Delta\varphi = \arg p$. The amplitude of the fringes would follow from $a \cdot b = |p|$ but it is of no interest in this context.

Sampling the interference fringes at three points is very easy, since the SLM introduces phase shifts into the wavefront anyway, meaning that an additional phase shift on the measured patch is straight forward to implement, and the whole scheme can be automated to display all phase patterns in a sequence and take measurements from the photodiode.

Figure 5.10 shows the great success of the presented scheme. Sub-figure a) shows the focal spot of the uncorrected optical system, which in addition to the parts shown in figure 5.8, contains two lenses for beam spreading and a mirror. The spot is highly distorted and it is obvious that a spot like this would lead to crosstalk, if several spots of this shape were placed close to each other. Sub-figure b) shows the focal spot after the obtained map of phase shifts is applied to the pattern, that yielded a). For this measurement 16×16 patches were measured. The shape of the focal spot is much more regular and the large rays have disappeared. Note that the scale of sub-figures a) and b) is exactly the same. The remaining spot size exactly matches the expected size, if the system was diffraction limited by the active surface of the SLM and the diffraction fringes fanning out to both sides and the top and bottom correspond exactly to diffraction from the SLMs rectangular surface. A calibration with 8×8 patches yielded a correction map after which aberrations, visible to the eye remained and a calibration with 32×32 patches did not improve the spot any further, compared to figure 5.10.

To implement this technique in an ion trap an appropriate quantity to infer the local intensity needs to be found. This can be the Rabi frequency Ω for the transition between the two states, coupled by the 729nm light.

For light polarized along the x axis, coupling, two states, denoted by $|1\rangle$ and $|2\rangle$ the Rabi frequency is

$$\Omega = \frac{e|\mathbf{E_0}|\langle 1|\,x\,|2\rangle}{\hbar} \tag{5.3}$$

with $|\mathbf{E_0}|$ the amplitude of the incident light. So with the Rabi frequency proportional to the square root of the intensity the latter can be extracted by measuring the former.

The complete set of measurements taken for this procedure took about 15 minutes, with $(16 \times 16 - 1) \times 3 = 765$ measurements taken, although optimization
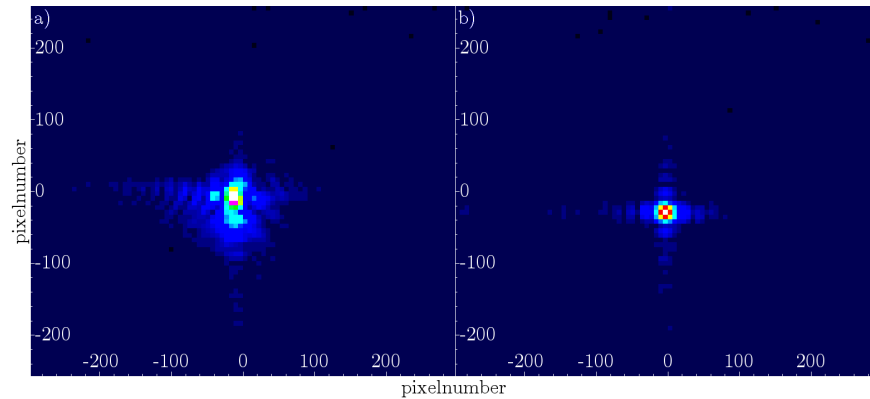
Figure 5.10: **Successful correction of aberrations in a test setup** Sub-figure a) shows the uncorrected focus spot, which shows heavy aberrations, which can cause crosstalk. Sub-figure b) shows the corrected spot, which is plotted on the same scale as the uncorrected. The much more regular shape is plainly visible.

would be possible in the scope of the test setup. If the technique were applied to the actual ion trap setup much longer measurement times are to be expected though since a single intensity measurement on an ion would take on the order of ten seconds instead of the roughly 1.2 seconds here.

5.3.2 Longterm stability

Suppose each measurement took 10 seconds, then the whole procedure would take about 128 minutes. This is hardly a procedure that can be run every day and not even every week. It is therefore desirable to know the longterm stability of the corrected beam. Since other measurements had been done in the meantime, the correction setup was built up anew and the correction procedure was run. For a period of 19 days the setup was unused and left untouched. The result is shown in figure 5.11. The uncorrected spot (a) shows heavy aberration, as before, while the corrected spot (b) is not quite as well corrected as in the measurement in the previous section. The spot shape after almost three weeks (c) shows slight degradation of the correction quality but it is still much more homogeneous than the uncorrected spot.

This shows that a correction measurement might not be necessary more than once a month and maybe even longer intervals are possible. However, more investigation might be needed, since during these 19 days no activity at all took place in our lab, which means, that climatic conditions were much more stable, compared to typical workdays.

An attempt to quantify the aberrations and their reduction in terms of the Zernike polynomials was made, but due to unexplained reflections inside the

wavefront reconstruction device spots of light appeared in the measurement region which made measuring the degree of aberration impossible. Although the problem was identified it could not be corrected and the reflections could not be reduced to an acceptable level, therefore the measurement had to be discarded.
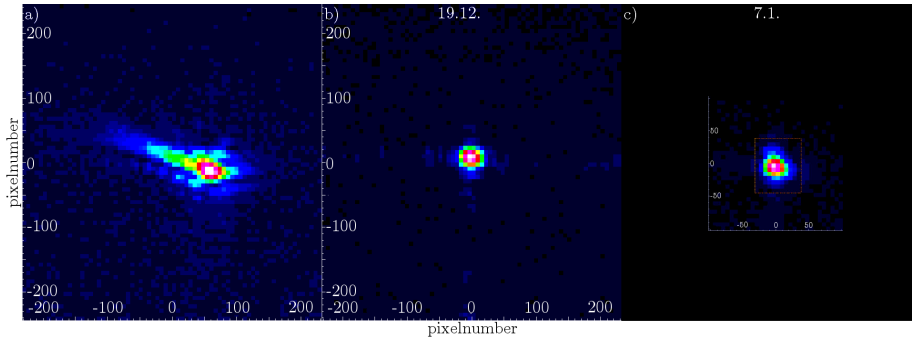

Figure 5.11: **Measurement of the longterm stability of the corrected beam** After a correction measurement (b) the system was allowed to rest for 19 days. While slight degradation of the corrected spot is visible (c) the overall quality is still highly improved, compared to the uncorrected spot (a). The third image was rescaled to fit the size of images (a) and (b).

5.4   Beam shaping capabilities

5.4.1   Further improvements to the MRAF algorithm

In section 3.7 it was shown, how to improve upon the basic iterative algorithm, by relaxing the constraints on the amplitude in the image plane. However, figure 3.13 d) shows, that the result of this improved algorithm is far from perfect. To further improve the algorithm's performance several tricks can be applied.
The two tricks revolve around the occurrence of speckle in the image plane, since the iterative algorithms cannot remove speckle selectively, but they can appear under the right circumstances. Speckle appear at optical vortices, that means in places, where the phase of the light changes by 2π over a very small distance. These can occur, if the initial guess for the phases, which is put into the algorithm, is created from random values. By choosing an appropriate initial guess for the phase pattern formation of speckle can be reduced.
While it is not possible to make a guess for the complex features of an output pattern, this being the necessity for the IFTA in the first place, it is relatively simple to create patterns, that create a spot of light in the output plane, which roughly matches the shape of the desired output. For example, patterns of the form $\phi(x, y) = ax^2 + by^2$ create a spot, with size depending on a and b. This is equivalent to a thin lens, effectively defocusing the light. Linear gradients of

the form $\phi(x, y) = ax + by$ shift the envelope and conical patterns of the form $\phi(x, y) = a\sqrt{x^2 + y^2}$ create a ring shaped output.

To observe the effects of these initial patterns they are simply Fourier transformed and the resulting image is overlapped with the target pattern. To also explore the possibilities in creating more complex patterns, an initial phase reconstruction for the batman symbol, with the resulting intensity distribution is shown in figure 5.12. One could say, the target of an initial phase pattern is to "nudge" the algorithm in the right direction. Also, the use of an analytical initial pattern avoids phase vortices, which are likely to occur if the initial phase pattern is random.

The next improvement, to reduce the formation of speckle, is the avoiding
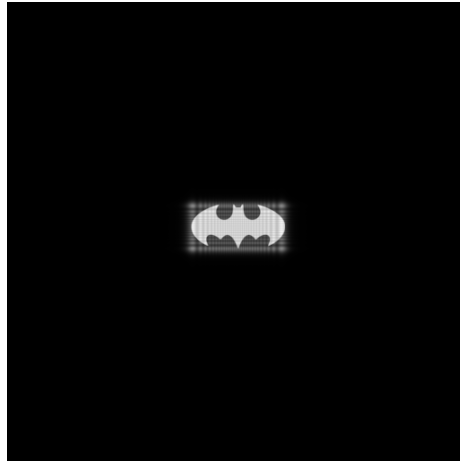

Figure 5.12: **Result of the initial guess for the phase pattern** By setting the parameters for a quadratic pattern, as well as a gradient, a spot is created, which roughly overlaps with the target image, which is shown as an overlay. For comparison the whole available image plane is depicted.

of points of zero intensity in the image plane. This is easily implemented, by setting the dark areas in the target image to a small nonzero value, instead of actual zero.

Figure 5.13 shows the reconstructed images of the pure MRAF algorithm and the refined algorithm, with an initial guess and nonzero dark areas. While the image on the left is dominated by speckle and has a high variation of average brightness over the whole pattern, the right image shows much improvement in both matters. Instead of optimizing the initial phase pattern by looking at figure 5.12 it is possible to watch the change in the reconstructed image with changed parameters. Figure 5.14 shows the result of this process. The left image shows the same reconstruction as figure 5.13 while on the right the "optimized" image can be seen. While the overall illumination of the pattern is more homogeneous, for example the edges of the wings are as bright as the inner part of the symbol, there is also an increase in irregularities in the pattern. Figure 5.15
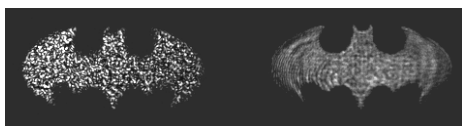
Figure 5.13: **Improved MRAF algorithm** To further improve the MRAF algorithm an initial guess was created for the phase pattern. Both images show the reconstructed images taken with a CCD camera. On the left the unrefined MRAF algorithm's performance is shown. Heavy speckle distorts the image and the brightness homogeneity is low. On the right, the reconstructed image, with the initial guess of the phase pattern is shown. The image suffers no more speckle and the brightness homogeneity is highly increased.
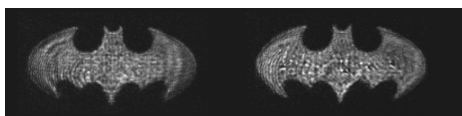

Figure 5.14: **Output for a complex pattern with modified initial guess** For the left image the initial phase pattern was adjusted in the way of figure 5.12. For the right image the reconstructed image was observed for each parameter change. While the overall illumination has improved, as can be seen in the brighter outer edges of the wings, the new pattern has more bumps.

shows a comparison of the spots from the two initial patterns of figure 5.14. The fact that the spot changes by a large amount through the optimization shows that great care needs to be taken, when finding the parameters for the initial phases. Simply creating a spot that overlaps with the target pattern may not be enough.

Blazed gratings and blaze condition

In the previous section's images the undiffracted light would always be visible as a bright spot in the center of the pattern. This limits the useful area of the hologram to its border regions. To remove this spot and thereby increase the usable area of the hologram, a grating can be added to the phase pattern, to diffract the hologram away from the center of the image plane and the undiffracted light.

Creating a discretized blazed grating in units of SLM pixels is straight forward. To get the shortest possible grating period every second row or column (or both, depending on the desired direction) needs to be shifted by π, compared to its neighbors. So for pixels, with coordinates i and j the equation for a diagonal grating would be

$$\phi(i,j) = (i+j) \bmod 2 \cdot \pi \tag{5.4}$$

yielding diagonal rows of 0 and π phase shift. This can be added to the calculated pattern. To maximize the light efficiency in this case it is advisable to
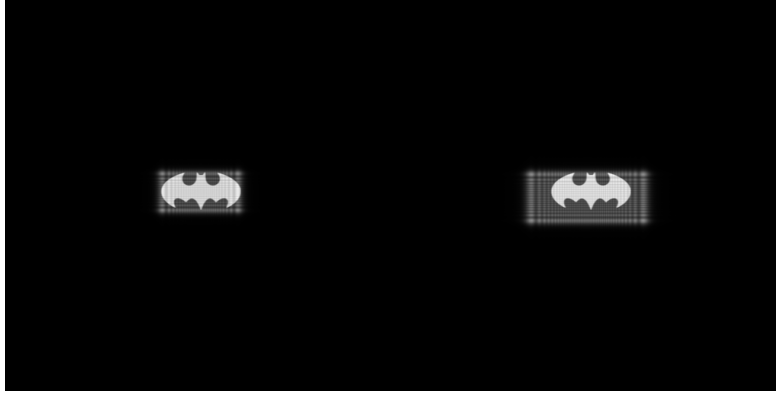
Figure 5.15: **Initial spots before and after optimization** The left and right images here correspond to the left and right images in figure 5.14. While increasing the size of the initial spot increases the homogeneity of the reconstructed image's brightness it also introduces more bumps. This trade-off needs to be considered when optimizing the initial pattern.

use a blazed grating and adjust the reflection angle of the SLM to fulfill the blaze condition. For ideal blazed gratings diffraction efficiency of 100% is in principle possible. However, for the SLM the efficiency is reduced, since not all light interacts with the liquid crystals.

For a reflective grating of line spacing d, as is shown in figure 5.16 the grating equation is:

$$d \left(\sin \alpha + \sin \beta\right) = m\lambda \tag{5.5}$$

with m the diffraction order and α and β the angles of incidence and diffraction. For a blazed grating with blaze angle ϑ_B the blaze condition is

$$\sin \left(\alpha - \vartheta_B\right) = \sin \left(\beta + \vartheta_B\right) \tag{5.6}$$

meaning, that light is reflected off the blaze steps into the same angle as it is diffracted into from the grating. Inserting the latter equation into the former and solving for α yields

$$\alpha = \sin^{-1} \left(\frac{m\lambda}{2d\cos\left(\vartheta_B\right)}\right) + \vartheta_B \tag{5.7}$$

While an ideal blazed grating is capable of reaching extremely high diffraction efficiencies there are several limiting factors to the light efficiency in an application.

First there is of course no ideal blazed grating. In the SLM the grating steps will always be discretized, although a longer grating period will result in more discretizing steps and therefore in a better approximation to the ideal grating. Second and more important is the fact that, especially for the MRAF algorithm,
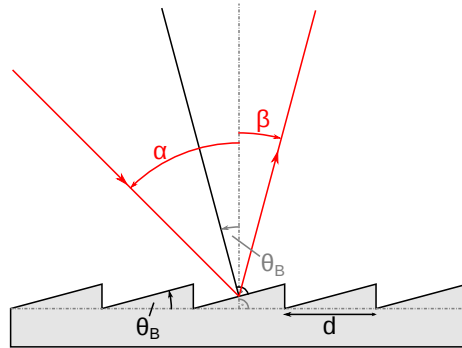
Figure 5.16: **Schematic depiction of a blazed reflection grating** Light incident under the angle α is diffracted into the angle β depending on the line spacing d of the grating. Depending on the blaze angle ϑ_B high diffraction efficiency for a wavelength can be achieved.

not all light, that gets diffracted off the SLM will be part of the desired pattern. In the noise region of the MRAF output, where the amplitudes are allowed to evolve freely peaks of high intensity will occur, which reduce the amount of light in the actually desired shape.

Third the intensity of a pattern reduces, with shrinking pattern size. One would expect the intensity to remain unchanged, if a top-hat of half the area is created, since intensity is power per area, however for small patterns the intensity seems to get smaller and smaller, which makes it hard to give a number for the absolute diffraction efficiency of the device.

5.5 Setup for integration with trap

Actual integration of the SLM with our ion trap setup requires a couple of extra features that need to be added to the basic testing setup. To access the ion trap in its vacuum vessel light is sent through a viewport, which provides a window with anti reflective coating. Figure 5.17 shows the vacuum vessel with its viewports. The viewport, chosen for the beam from the SLM is seen at the top of the drawing. While having the advantage of light from this viewport hitting the trap perpendicular to the trap axis it is also very far from the trap. The distance from the window's outer edge to the trap axis is 394mm. Together with the fact that the SLM can, for spatial reasons, not be setup to reflect light directly into the viewport this means, that a lens with high focal length will be necessary in this setup. However, from equation 3.45 follows a size of the image of 2.43cm, with an assumed focal length of 500mm. Since the smallest feature, that can be defined in the target image for the MRAF algorithm is $1/512$ times the image size, no structures, smaller, than $47.5\mu m$ can be defined. So irrespective of the actual resolution of the lens, which mostly depends on its diameter, only three pixels in the target image would define a structure, which
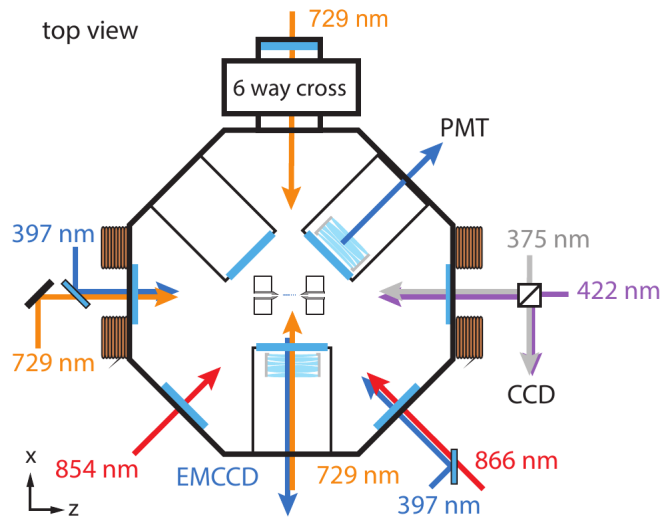
Figure 5.17: **Schematic drawing of the vacuum vessel, with its viewports and corresponding in and outputs.** The viewport, which can be used for the SLM is entering the vessel from the top in this picture. The distance from the window to the center of the trap is 394mm.

would illuminate the entire string of ions, depicted in figure 2.3.

While this may seem purely a problem of convenience one should also note, that the smallest spot size, possible with a 2 inch lens of 500mm focal length is 18.3μm in diameter. It is obvious, that using a single lens of 500mm focal length would be wasting its resolving power.

A solution to this problem would be using a relay lens setup. In such a setup a primary lens creates a real image at a certain distance and one or two relay lenses are used to create another image, without magnification, at a larger distance, thereby relaying the original image. The two possible relay lens setups are depicted in figure 5.18. The advantage of the setup with two lenses in the relay is, that the position of the relayed image can be adjusted, by moving the second relay lens. To do so in the setup with only on relaying lens both the imaging lens as well as the relaying lens would need to be moved, since their distance is fixed by their focal lengths. Using two lenses for relaying is therefore more flexible, which is an important point in a setup, where the image plane, viz. the trap axis, can not be moved at all.

Using an imaging lens of 200mm focal length would create an image of 9.72mm length, yielding a smallest definable feature of 19μm. Now an ion string as mentioned above would correspond to a chain of six pixels in the target image. Taking into account, that the actual diameter of the light incident on the lenses is limited by the aperture of the SLM, the spot sizes change.

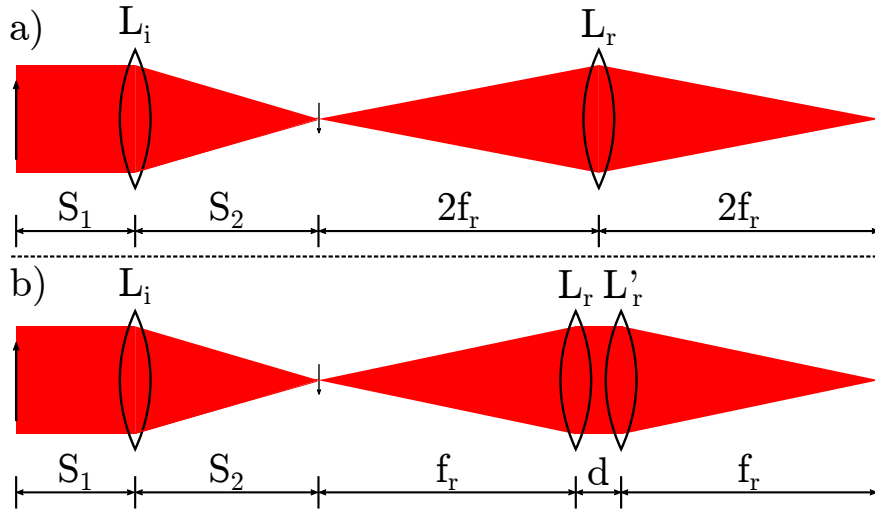With an imaging lens of 200mm focal length the smallest spot is at 24.2μm,

Figure 5.18: **Two possible setups for relay lenses** While the first setup uses only one lens and relays the image by a distance of $4f_r$ it has reduced flexibility in the positioning of the focal point. Using two lenses for the relay system creates a relay distance of $2f_r + d$. Since the distance d between the lenses is arbitrary the focal plane can be adjusted.

assuming an incident Gaussian beam of 7.68mm diameter, which would exactly fit into the SLM's active region. Relaying this with a lens of f=500mm yields the same spot size in the image plane, since the beam does not extend beyond the size of the relay lens in that setup.

Figure 5.19 shows a possible setup for illuminating the SLM, creating an image and relaying it into the trap. The lenses for the appropriate illumination of the SLM need to be chosen according to the beam from the fiber coupler. The angle α between the incident and reflected light at the SLM need to be chosen such, that the blaze condition is fulfilled for the first diffracting order, to maximize light efficiency. To adjust the focal plane of the second relay lens it can be mounted on a translation stage to move it along the beam axis. The mirror, reflecting the light through the window should have a small transmittivity, to allow monitoring the created pattern with a CCD camera, behind the mirror. To adjust the mirror with high enough precision it can be put into a mount with motorized actuators. A mirror mount like that is currently in use in precisely this position and can be reused in this setup.
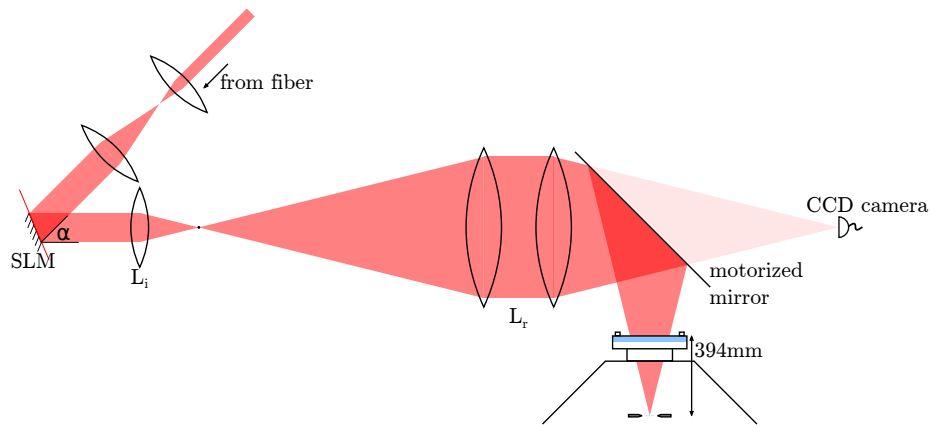
Figure 5.19: **Suggested setup for integration of the SLM with the existing ion trap setup** To bridge the distance of 394mm from the vaccum window to the trap relay lenses of $f_r = 500$mm should be used, to leave enough space for the mirror and to provide freedom for adjustment. A mirror with small transmission, on the order of a few percent would allow the placement of a CCD camera, to observe the created patterns and employ feedback techniques in situ.

Chapter 6

Conclusion and Outlook

In this thesis a spatial light modulator of the liquid crystal type was introduced and characterized. The theoretical background of its operation was introduced and derived. Different algorithms to calculate holograms for the device were implemented and compared. An interferometric calibration was performed, to assure correct performance of the device. Furthermore it was shown how to perform in situ correction of optical aberrations in an ion trap setup, potentially up to diffraction limited performance. Finally a setup for integration of the device with the existing ion trap setup in our laboratory was suggested.

As soon as the current experiments in the lab are finished the SLM should be integrated with the setup, to put to the test the capabilities in improving the homogeneous illumination of an ion string. Together with a feedback scheme, to reduce residual inhomogeneities, large improvement over the current setup with cylindrical lenses should be possible.

Appendix A

Semi-classical treatment of light-atom interaction

In this section a more detailed introduction to the theory of the interaction of atoms with light will be given. This treatment follows chapter seven of [7].

This is a so called semi-classical treatment of the problem, meaning that it is in part classical and in part quantum mechanical. Here a quantum mechanical two level system shall be considered, while the light, interacting with it will be treated classically. Also the aforementioned concepts of the Rabi frequency and the Bloch sphere will be derived.

Assuming a Hamiltonian of the form

$$H = H_0 + H_I(t) \tag{A.1}$$

with H_0 the Hamiltonian of the unperturbed atom and H_I the Hamiltonian of the light field, the discussion starts by stating the wave functions for the time dependent Schrödinger equation

$$i\hbar \frac{\partial \Psi}{\partial t} = H\Psi \tag{A.2}$$

for the unperturbed atom:

$$\Psi_n(\mathbf{r}, t) = \psi(\mathbf{r}) e^{-iE_n t/\hbar} \tag{A.3}$$

While these wave functions are not eigenfunctions of the full Hamiltonian, its wave function can be expressed through these for any point in time by:

$$\Psi(\mathbf{r}, t) = c_1(t) \psi_1(\mathbf{r}) e^{-iE_1 t/\hbar} + c_2(t) \psi_2(\mathbf{r}) e^{-iE_2 t/\hbar} \tag{A.4}$$

or, in Dirac notation

$$\Psi(\mathbf{r}, t) = c_1 |1\rangle e^{-i\omega_1 t} + c_2 |2\rangle e^{-i\omega_2 t} \tag{A.5}$$

with $\omega_n = E_n/\hbar$ and $|c_1|^2 + |c_2|^2 = 1$.

Assuming an electric field of $\mathbf{E} = \mathbf{E}_0 \cos(\omega t)$, the interaction term H_I takes the form of a dipole in an electric field:

$$H_I(t) = e\mathbf{r} \cdot \mathbf{E}_0 \cos(\omega t) \tag{A.6}$$

with $\mathbf{r}$ the position of the electron, with respect to the atomic nucleus. This term will lead to an interaction and with that mixing of the unperturbed eigenstates of the atom. Substituting equation A.5 into the time dependent Schrödinger equation yields

$$i\dot{c}_1 = \Omega \cos(\omega t) e^{-i\omega_0 t} c_2 \tag{A.7}$$

$$i\dot{c}_2 = \Omega \cos(\omega t) e^{-i\omega_0 t} c_1 \tag{A.8}$$

with $\omega_0 = (E_2 - E_1)/\hbar$ and Ω the Rabi frequency, given by:

$$\Omega = \frac{\langle 1| e\mathbf{r} \cdot \mathbf{E}_0 |2 \rangle}{\hbar} = \frac{e}{\hbar} \int \psi_1^*(r) \mathbf{r} \cdot \mathbf{E}_0 \psi_2(r) d^3\mathbf{r} \tag{A.9}$$

Limiting this discussion to light, polarized along the x-axis, yielding $\mathbf{E} = |\mathbf{E}_0|\hat{e}_x \cos(\omega t)$, the Rabi frequency becomes

$$\Omega = \frac{eX_{12}|\mathbf{E}_0|}{\hbar} \tag{A.10}$$

with $X_{12} = \langle 1| x |2 \rangle$ the overlap of the two wave functions along the x axis. In the case of all population starting in $|1\rangle$, viz $c_1(0) = 1$ and $c_2(0) = 0$ an approximation for small times, that means, only little population transfer can be obtained from equations A.7 and A.8:

$$c_1(t) = 1 \tag{A.11}$$

$$c_2(t) = \frac{\Omega^*}{2} \left\{ \frac{1 - \exp\left[i(\omega_0 + \omega)t\right]}{\omega_0 + \omega} + \frac{1 - \exp\left[i(\omega_0 + \omega)t\right]}{\omega_0 - \omega} \right\} \tag{A.12}$$

An important approximation can be made here: Seeing that for the case close to resonance, $|\omega_0 - \omega| \ll \omega_0$ the first denominator is approximately $2\omega_0$ while the second approaches zero. This means that the first term will be much smaller, than the second and can therefore be neglected. This is known as the *rotating-wave approximation* and it yields an equation for finding the electron in the upper state of the two-level system:

$$|c_2(t)|^2 = \left| \Omega \frac{\sin\{(\omega_0 - \omega)t/2\}}{\omega_0 - \omega} \right|^2 \tag{A.13}$$

While this was an assumption for weak fields, the more general case is obtained, by rewriting equation A.7 as

$$i\dot{c}_1 = c_2 \left\{ e^{i(\omega - \omega_0)t} + e^{-i(\omega + \omega_0)t} \right\} \frac{\Omega}{2} \tag{A.14}$$

and equation A.8 accordingly. Applying the rotating-wave approximation again and combining the two differential equations yields:

$$\frac{d^2 c_2}{dt^2} + i\left(\omega - \omega_0\right)\frac{dc_2}{dt} + \left|\frac{\Omega}{2}\right|^2 c_2 = 0 \tag{A.15}$$

And from this, by setting $W^2 = \Omega^2 + \left(\omega - \omega_0\right)^2$ the following is obtained

$$\left|c_2\left(t\right)\right|^2 = \frac{\Omega^2}{W^2}\sin^2\left(\frac{Wt}{2}\right) \tag{A.16}$$

or at resonance, viz. $W = \Omega$

$$\left|c_2\left(t\right)\right|^2 = \sin^2\left(\frac{\Omega t}{2}\right) \tag{A.17}$$

It follows, that the population will oscillate between the two states, depending on the length of the interaction with the light. Two special cases of this formula are notable: If $\Omega t = \pi$ the populations of $|1\rangle$ and $|2\rangle$ will be exchanged:

$$c_1\left|1\right\rangle + c_2\left|2\right\rangle \rightarrow -i\left(c_2\left|1\right\rangle + c_1\left|2\right\rangle\right) \tag{A.18}$$

The other case is $\Omega t = \pi/2$, which will bring a population from the ground state to an equal superposition of both states. These two cases are called π- and $\pi/2$-pulses.

The Bloch sphere

To derive the Bloch sphere representation of the atomic state again an electric field along the x-axis is assumed and the component of a dipole along this axis shall be calculated. It is given by the expectation value:

$$-eD_x\left(x\right) = -\int \Psi^\dagger\left(t\right) e \cdot x \Psi\left(t\right) d^3\mathbf{r} \tag{A.19}$$

Using equation A.4 for Ψ yields the dipole moment:

$$D_x\left(t\right) = \int \left(c_1 e^{-i\omega_1 t}\psi_1 + c_2 e^{-i\omega_2 t}\psi_2\right)^* x \left(c_1 e^{-i\omega_1 t}\psi_1 + c_2 e^{-i\omega_2 t}\psi_2\right) d^3\mathbf{r} \tag{A.20}$$

$$= c_2^* c_1 X_{21} e^{i\omega_0 t} + c_1^* c_2 X_{12} e^{-i\omega_0 t} \tag{A.21}$$

with $\omega_0 = \omega_2 - \omega_1$. The quantities $c_1^* c_2$ and $c_2^* c_1$ can be obtained from the density matrix formalism:

$$\left|\Psi\right\rangle\left\langle\Psi\right| = \begin{pmatrix} c_1 \\ c_2 \end{pmatrix}\begin{pmatrix} c_1^* & c_2^* \end{pmatrix} = \begin{pmatrix} \left|c_1\right|^2 & c_1 c_2^* \\ c_2 c_1^* & \left|c_2\right|^2 \end{pmatrix} = \begin{pmatrix} \rho_{11} & \rho_{12} \\ \rho_{21} & \rho_{22} \end{pmatrix} \tag{A.22}$$

Here, the diagonal elements are called populations and the off diagonal elements are the so called coherences. Defining

$$\widetilde{c}_1 = c_1 e^{-i\delta t/2} \tag{A.23}$$

$$\widetilde{c}_2 = c_2 e^{i\delta t/2} \tag{A.24}$$

with $\delta = \omega - \omega_0$ the detuning of the light from the atomic resonance. While the populations stay unaffected by this transformation, the coherences become,

$$\widetilde{\rho}_{12} = \rho_{12} e^{-i\delta t} \tag{A.25}$$

$$\widetilde{\rho}_{21} = \rho_{21} e^{i\delta t} \tag{A.26}$$

yielding a dipole moment of

$$-eD_x(x) = -eX_{12}\left\{\rho_{12}e^{i\omega_0 t} + \rho_{21}e^{-i\omega_0 t}\right\} = -eX_{12}\left\{\widetilde{\rho}_{12}e^{i\omega t} + \widetilde{\rho}_{21}e^{-i\omega t}\right\} \tag{A.27}$$

$$= -eX_{12}\left\{u\cos\omega t - v\sin\omega t\right\} \tag{A.28}$$

Where $u = \widetilde{\rho}_{12} + \widetilde{\rho}_{21}$ and $v = -i\left(\widetilde{\rho}_{12} - \widetilde{\rho}_{21}\right)$ are the real and imaginary parts of $\widetilde{\rho}_{12}$.

Next the differential equations from the beginning are written in terms of δ:

$$i\dot{c}_1 = c_2 e^{i\delta t}\frac{\Omega}{2} \tag{A.29}$$

$$i\dot{c}_2 = c_1 e^{-i\delta t}\frac{\Omega}{2} \tag{A.30}$$

Differentiating equation A.23 and using equations A.23, A.24, A.29 and A.30 the following equations can be obtained:

$$i\dot{\widetilde{c}}_1 = \frac{1}{2}\left(\delta\widetilde{c}_1 + \Omega\widetilde{c}_2\right) \tag{A.31}$$

$$i\dot{\widetilde{c}}_2 = \frac{1}{2}\left(\Omega\widetilde{c}_1 - \delta\widetilde{c}_2\right) \tag{A.32}$$

From these the time derivatives of the density matrix components are obtained:

$$\frac{d\widetilde{\rho}_{12}}{dt} = \left(\frac{d\widetilde{\rho}_{21}}{dt}\right)^* = -i\delta\widetilde{\rho}_{12} + \frac{i\Omega}{2}\left(\rho_{11} - \rho_{22}\right) \tag{A.33}$$

$$\frac{d\rho_{22}}{dt} = \frac{d\rho_{11}}{dt} \tag{A.34}$$

By using $w = \rho_{11} - \rho_{22}$ and expressing the above equations in terms of u, v and w, the following equations are obtained:

$$\dot{u} = \delta v \tag{A.35}$$

$$\dot{v} = -\delta u + \Omega w \tag{A.36}$$

$$\dot{w} = -\Omega v \tag{A.37}$$

These equations can be written in vectorial form, as

$$\dot{\mathbf{R}} = \mathbf{R} \times (\Omega \hat{e}_1 + \delta \hat{e}_3) = \mathbf{R} \times \mathbf{W} \qquad (A.38)$$

with the *Bloch vector*:

$$\mathbf{R} = u\hat{e}_1 + v\hat{e}_2 + w\hat{e}_3 \qquad (A.39)$$

and

$$\mathbf{W} = \Omega \hat{e}_1 + \delta \hat{e}_3 \qquad (A.40)$$

The vector $\mathbf{R}$ has length one, so $|\mathbf{R}|^2 = |u|^2 + |v|^2 + |w|^2 = 1$. Accordingly the vector points to the surface of the unit sphere, the *Bloch sphere*, which is depicted in figure A.1. It follows from equation A.38 that the product $\mathbf{R} \cdot \mathbf{W} = RW \cos\theta$ is constant. So for a fixed detuning and Rabi frequency R and W are constant and the Bloch vector will move on a cone with angle θ around $\mathbf{W}$.

Especially in the case of no detuning ($\delta = 0$) and the initial population in the state $|1\rangle$ the Bloch vector will rotate on the great circle on the plane perpendicular to $\hat{e}_1$, which is equivalent to the coherent population transfer, as seen in the previous section.
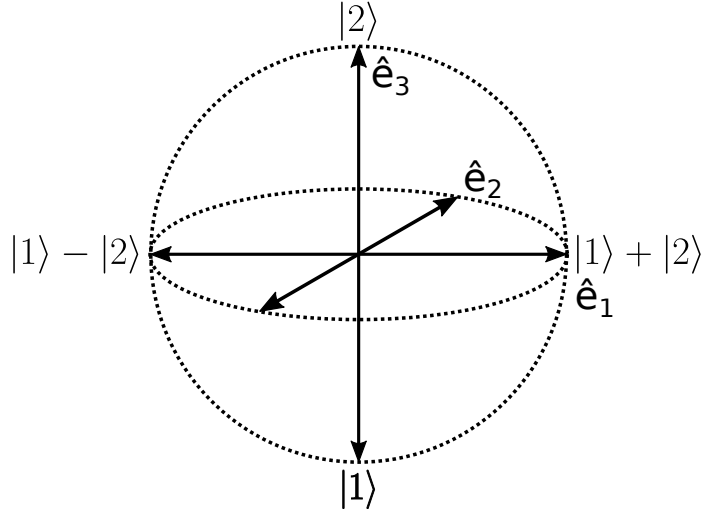

Figure A.1: **The Bloch sphere** The states of a two level system can be encoded in the surface of a sphere, which makes it easy to visualize the concepts of π- and $\pi/2$-pulses, as well as more complicated sequences. An interesting, although unintuitive feature of the Bloch sphere representation is the fact that orthogonal vectors point to opposite points on the surface of the sphere.

Acknowledgements

- I would like to thank Prof. Blatt for giving me the opportunity to write my Master's thesis in his group.

- I would also like to thank Prof Weinfurter in making this enterprise possible.

- Next I would like to thank Christian Roos and Cornelius Hempel for supervising my work and providing help and insights whenever I needed them.

- I also would like to thank my colleagues from the Quantum Simulation, Precision and Ultrafast experiments for creating a wonderful working environment.

- Last but not least I would like to thank my family and friends who make my time worthwhile.

Bibliography

[1] Born and Wolf. *Principles of Optics*. Cambridge University Press, seventh (expanded) edition, 1999.

[2] J. I. Cirac and P. Zoller. Quantum computations with cold trapped ions. *Phys. Rev. Lett.*, 74:4091–4094, May 1995.

[3] D. P. DiVincenzo. The physical implementation of quantum computation. *Fortschritte der Physik*, 48(9-11):771–783, 2000.

[4] A. Einstein, B. Podolsky, and N. Rosen. Can quantum-mechanical description of physical reality be considered complete? *Phys. Rev.*, 47:777–780, May 1935.

[5] R. P. Feynman. Simulating physics with computers. *International Journal of Theoretical Physics*, 21(6-7):467–488, 1982.

[6] J. R. Fienup. Phase-retrieval algorithms for a complicated optical system. *Appl. Opt.*, 32(10):1737–1746, Apr 1993.

[7] C. Foot. *Atomic physics*. Oxford master series in physics. Oxford University Press, 2005.

[8] D. Gabor. A new microscopic principle. *Nature*, 161(4098):777–778, 1948.

[9] R. Gerchberg and W. Saxton. Practical algorithm for determination of the phase frrom image and diffraction plane pictures. *Optik*, 35(2):237, 1972.

[10] J. Goodman. *Introduction to Fourier Optics*. McGraw-Hill Series in Electrical and Computer Engineering: Communications and Signal Processing. McGraw-Hill, 1996.

[11] G. Green. *An Essay on the Application of Mathematical Analysis to the Theories of Electricity and Magnetism*. Göteborg: Wezäta-Melins 1958. author, 1828.

[12] D. Griffiths. *Introduction to Elementary Particles*. Wiley, 2008.

[13] Q. Gu, C. Wu, S. Chen, and Y. Huang. Direct decoration of disclinations by solidification-induced band texture and focal-conic texture for a low molar mass liquid crystal. *Liquid Crystals*, 30(2):117–123, 2003.

[14] C. Hempel. *Digital quantum simulation, Schrödinger cat state spectroscopy and setting up a linear ion trap.* PhD thesis, University of Innsbruck, 2014.

[15] B. N. S. Inc. *Spatial Light Modulators - XY Series Datasheet.*

[16] B. N. S. Inc. *User Manual - Standard XY Phase Series Spatial Light Modulator With DVI Controller.* Boulder Nonlinear Systems, Inc., January 2011.

[17] H. Kawamoto. The history of liquid-crystal displays. *Proceedings of the IEEE*, 90(4, SI):460–500, APR 2002.

[18] N. A. Lockwood, J. K. Gupta, and N. L. Abbott. Self-assembly of amphiphiles, polymers and proteins at interfaces between thermotropic liquid crystals and aqueous phases. *Surface science reports*, 63(6):255–293, JUN 15 2008.

[19] M. Pasienski and B. DeMarco. A high-accuracy algorithm for designing arbitrary holographic atom traps. *Opt. Express*, 16(3):2176–2190, Feb 2008. MRAF.

[20] T. Poon and J. Liu. *Introduction to Modern Digital Holography: With Matlab.* Cambridge University Press, 2014.

[21] A. Sørensen and K. Mølmer. Quantum computation with ions in thermal motion. *Phys. Rev. Lett.*, 82:1971–1974, Mar 1999.

[22] Strobl. *Condensed matter physics.* Springer-Verlag, 2004. ISBN: 978-3540003533.

[23] G. Thalhammer. Private communication.

[24] G. Thalhammer, R. W. Bowman, G. D. Love, M. J. Padgett, and M. Ritsch-Marte. Speeding up liquid crystal slms using overdrive with phase change reduction. *Opt. Express*, 21(2):1779–1797, Jan 2013.

[25] V. Venediktov, G. Nevskaya, and M. Tomilin. Liquid crystals in dynamic holography (review). *Optics and Spectroscopy*, 111(1):113–133, 2011.

[26] J. P. Waters. Holographic image synthesis utilizing theoretical methods. *Applied Physics Letters*, 9(11):405–407, 1966.

[27] P. Zupancic. Dynamic holography and beamshaping using digital micromirror devices. Master's thesis, LMU München, 2013.

Erklärung:

Hiermit erkläre ich, die vorliegende Arbeit selbständig verfasst zu haben und keine anderen als die in der Arbeit angegebenen Quellen und Hilfsmittel benutzt zu haben.

München, 26. Mai 2015